Physics – Uspekhi **54** (5) 473 – 498 (2011)

REVIEWS OF TOPICAL PROBLEMS PACS numbers: **66.30.–h**, 68.35.Fx, **68.65.–k**

Reactive diffusion in multilayer metal/silicon nanostructures

E N Zubarev

DOI: 10.3367/UFNe.0181.201105c.0491

Contents

Abstract. Reactive diffusion in nanomaterials differs widely from that in bulk materials. Reviewed in this paper are the basic models and experimental data on how diffusion and phase transformations occur in multilayer nanosystems as these are being prepared and subsequently thermally annealed. The growth kinetics of amorphous silicide phases in Sc/Si and Mo/Si multilayer periodic systems are studied using the combination of high-resolution transmission electron microscopy and small-angle X-ray diffraction. A model is proposed for silicon diffusion through amorphous silicide that undergoes structural relaxation and crystallization as it grows. Anisotropic diffusion and growth of the silicide phase at adjacent interfaces are studied, and the diffusion parameters are measured for the earliest stages of diffusion annealing.

E N Zubarev National Technical University
'Kharkiv Polytechnical Institute',
Frunze st. 21, 61002 Kharkiv, Ukraine
Tel. (+38-057) 707 61 81. Fax (+38-057) 700 40 34
E-mail: zubar@kpi.kharkov.ua

Received 24 June 2010
Uspekhi Fizicheskikh Nauk **181** (5) 491 – 520 (2011)
DOI: 10.3367/UFNr.0181.201105c.0491
Translated by Yu V Morozov; edited by A Radzig

1. Introduction

Diffusion and phase formation in transition metal/silicon film systems have important practical implications. Silicides of transition metals are extensively used in the modern silicon semiconductor industry by virtue of their low resistivity and rather high melting temperature. Schottky diodes, ohmic contacts with shallow active elements of very large-scale integrated circuits, and low-resistance high-temperature thin-film interconnects between elements are only few examples of silicide applications in modern microelectronics. The practical value of transition metal silicides stimulated numerous experimental studies of diffusion and phase formation in metal/silicon systems. Diagrams of metal/silicon binary systems display a number of solid solutions and intermediate phases (silicides). The chemical potential gradient at the metal/silicon interface provides the driving force for component mixing. It was noticed that amorphous intermixed zones at the metal/silicone interface appear in early stages of metallic film deposition on mono-, poly-, and amorphous silicon at low temperatures. What are their composition and mechanism of formation? What are the growth kinetics of the intermediate silicide phase during isothermal annealing and how do they depend on the structure and mechanical stress of metal and silicon layers? What element is the dominant diffusant and what is the silicide into which the amorphous intermediate phase crystal-

lizes? All these issues are of significant interest for scientists engaged in basic and applied research on silicon materials.

Certain periodic metal/silicon multilayer structures find wide application as reflective elements in extreme UV optics ($1 \leqslant \lambda \leqslant 50$ nm) due to their high reflection coefficients obtained in experiment. In recent years, considerable progress has been achieved in manufacturing high-reflectance Mo/Si multilayer X-ray mirrors perspective for using in 13.4-nm X-ray lithography and astrophysical research. Significant effort has been directed to gaining insight into the real structure of these periodic multilayer coatings (PMCs) both before and after annealing. Sc/Si PMCs with a period of 20–35 nm are promising candidates for application as mirrors in the wavelength range $35 \leqslant \lambda \leqslant 50$ nm. Specifically, they have been employed to control X-ray laser radiation at $\lambda = 46.9$ nm, in X-ray microscopy, and in astrophysical surveys. The optical properties of multilayer X-ray mirrors strongly depend on the presence of intermediate phase interlayers at interfaces between the starting materials. This fact gave an additional impetus to investigations into diffusion and phase formation processes in metal/silicon multilayer structures.

Since metal/silicon layered structures used as microelectronic devices and optical elements for soft X-ray range have nanoscale layer thickness, the study of early diffusion and phase formation stages in these systems is indispensable for understanding their properties. Moreover, periodic multilayer coatings proved to be very convenient model objects for the exploration of diffusion and silicide formation processes. In terms of diffraction, such coatings are artificial one-dimensional crystals. Small-angle X-ray reflectivity (SAXR) from layer boundaries is highly sensitive to the slightest structural changes in interphase boundaries. This makes it possible to accurately determine the thickness of both intermediate phases and pure components. High-resolution cross-sectional transmission electron microscopy (TEM) is a complementary method for studying phase interfaces. It permits elucidating the structure of individual layers and verifying theoretical predictions based on SAXR spectra. The combination of small-angle X-ray diffractometry and cross-sectional TEM opens up better than ever the opportunity to study diffusion and phase formation at the atomic level.

2. Theoretical models describing the initial stages of interphase reactions

2.1 The Bene–Walser rule

Diffusive mass transfer during annealing of a binary diffusion pair ensures that the thermodynamic system seeks an equilibrium. It accounts for the unique correspondence between the equilibrium diagram and the diffusion zone. Given the extended diffusion zone and prolonged diffusion annealing time, the zone must consist of phase layers whose chemical composition and sequence are consistent with the phase equilibrium diagram [1–3]. If a binary system contains several phases, the natural question arises of which phase is the first to form at the interface between the primary components. This question acquires special significance in thin-film technologies, where the diffusion zone is only a few nanometers thick, e.g., in periodic multilayer compositions that find application in soft X-ray optics. In this case, the first phase that forms and grows on interphase boundaries during isothermal annealing may be the sole one till one of the components is completely consumed. Not infrequently, amorphous layers initially formed at the metal/silicon interphase boundaries become thick enough to undergo crystallization into metastable high-temperature phases [4] that transform into stable ones in the course of further higher-temperature annealing.

During the past decades, a considerable body of experimental data have been collected about silicide formation and growth [5, 6]. Bene and Walser undertook an analysis of the voluminous experimental material on metal silicides (16 binary metal/silicon systems) and proposed an empirical rule for the selection of the first phase, based on the phase diagram [7]. The rule originates from the assumption that the amorphous phase (glass membrane) formed at the *Me*/Si interface at the initial moment has a composition corresponding to the lowest-melting eutectic. Later on, the glass membrane crystallizes into a congruently melting silicide adjacent to the lowest-melting eutectic and having the highest melting temperature. This rule has a good physical grounding. First, low-melting eutectics ensure faster mass transfer due to a high diffusion coefficient. As is known, the activation energy for substitutional diffusion is directly proportional to the melting temperature [8]. For this reason, if several phase nuclei simultaneously arise at the interface, the lowest-melting phase must grow more rapidly and suppress the growth of other phases having different chemical composition. Therefore, the phase selection at the initial stages is governed by kinetic factors. Second, the formation of a higher-melting silicide subject to congruent melting gives a higher free energy gain in the system. In this case, selection of the crystalline silicide is already limited by thermodynamic factors. The authors argue that a glass–congruent silicide transition requires a smaller short-range rearrangement and, consequently, a lower energy barrier.

Although this rule correctly predicts the first silicide in many *Me*/Si systems, it has exceptions and remains debatable [6]. To begin with, it is based on the assumption that a stable amorphous phase with a sufficiently narrow concentration range forms at the *Me*/Si interface. It is known, however, that the concentration interval of binary amorphous alloys obtained by the vacuum condensation method may be rather wide [9]. Second, the rule appears to be ambiguous if applied to certain systems, e.g. Pt/Si , which makes it difficult to choose between Pt_3Si and Pt_2Si silicides. Both are located on one side of the deep eutectic point in the equilibrium diagram, with Pt_2Si being a higher-melting silicide, and Pt_3Si being closer to the eutectic concentration. Third, the rule gives wrong predictions for such binary systems as Ti/Si, Mn/Si, and Zr/Si. Moreover, it disregards the thickness of the amorphous membrane being formed at the very beginning of diffusion interaction at the *Me*/Si interface. Also unknown is the critical thickness of the amorphous phase at which its crystallization and the formation of the first crystalline silicide take place. More experiments are needed to clarify these issues.

The Bene–Walser rule correctly predicts the formation of molybdenum disilicide, $MoSi_2$, in a binary Mo/Si system; however, it is inapplicable to the Sc/Si system also considered in the present work. In accordance with the phase diagram, Sc_3Si_5 silicide is closest to the lowest-melting eutectic ($Sc_3Si_5 + Si$). This and two more silicides, ScSi and Sc_5Si_4, have incongruent melting points. Finally, scandium-richest silicide Sc_5Si_3 is the sole silicide to undergo congruent melting,

but it is adjacent to a different, higher-melting eutectic ($Sc_5Si_3 + Sc$). It is worth mentioning that the difference between melting temperatures of eutectics does not exceed 20 °C. Bearing in mind the current state of the theory for Sc/Si type systems, there is only one opportunity (experiment) to determine which silicide is the first to form in the diffusion zone and to elucidate the sequence of formation of other silicides.

2.2 The Gösele and Tu kinetic approach

Certain thin-film metal/silicon diffusion pairs (the case of thin films) do not contain all the intermediate silicide phases present in the equilibrium diagram [5, 6]. As a rule, only one of the phases is observed in experiment. For example, an Ni/Si diffusion pair contains Ni_2Si silicide at a temperature above 200 °C. Other equilibrium silicides — Ni_3Si, Ni_3Si_2, Ni_5Si_2, NiSi, and $NiSi_2$ — are not formed in the diffusion zone subject to the condition that their primary components remain unexhausted. For thicker diffusion pairs, e.g., thicker than 10 μm (the bulk case), the diffusion space contains all intermediate equilibrium phases predicted by the equilibrium diagram. Gösele and Tu [10] studied the influence of reaction barriers at interphase boundaries on phase growth kinetics in the diffusion zone. Figure 1 illustrates the idea behind their experiment. The growth kinetics of the layer of an intermediate compound is governed by two processes:

(1) transport of atoms of the primary components toward the reaction site (the boundary between the intermediate compound and the pure components, where the chemical reaction runs, giving rise to an additional layer of the intermediate compound);

(2) local atomic rearrangement at the interphase boundary (reconstruction) necessary for producing a chemical compound with the intrinsic short-range order; it implies overcoming the reaction barrier.

Hence, there are two assumptions (two types of growth kinetics of the intermediate compound). Given that diffusion is a slower process limiting the growth rate of the intermediate compound, its kinetics is referred to as diffusionally controlled, and the layer thickness is proportional to the square root of the diffusion annealing time. If it is the reaction barriers at interphase boundaries that control growth kinetics, such kinetics is called boundary or reaction-controlled.

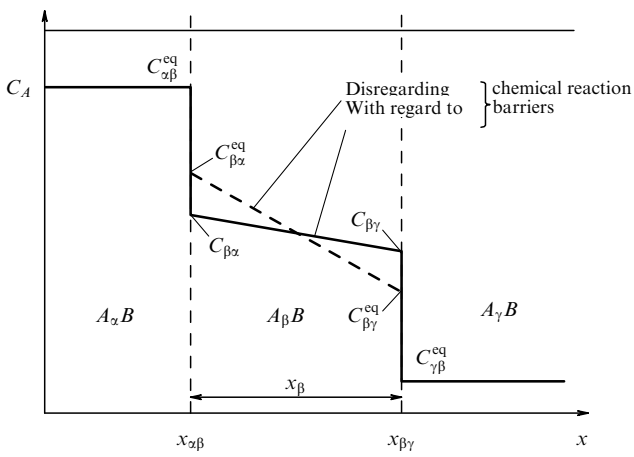

Figure 1. Schematic concentration profile of A atoms in the diffusion space, $A_\alpha B/A_\beta B/A_\gamma B$ ($\alpha > \beta > \gamma$), without and with account of the chemical reaction barrier [24]. $A_\beta B$ phase is the intermediate compound. $C^{eq}_{\beta\alpha}$ is the equilibrium concentration .

The following characteristic time dependences determine which of the two mechanisms prevails:

$$x_\beta \sim t \quad \text{for} \quad x_\beta \ll x^*_\beta\,, \tag{1}$$

$$x_\beta \sim t^{1/2} \quad \text{for} \quad x_\beta \gg x^*_\beta\,, \tag{2}$$

where x_β is the intermediate phase thickness, x^*_β is the critical intermediate phase thickness, and t is the isothermal annealing time.

The critical thickness of the intermediate phase is given by the ratio of the diffusion coefficient of pure components across the intermediate compound layer ($\tilde{D}$) to the effective reaction barrier (k_{eff}) at either interface between the intermediate compound and the pure components:

$$x^*_\beta = \frac{\tilde{D}}{k_{\text{eff}}}\,. \tag{3}$$

The authors of Ref. [10] analyzed the behavior of two hypothetical compounds in the diffusion space in the following situations:

(1) diffusion-controlled growth of both phases;

(2) reaction-controlled growth of both phases;

(3) diffusion-controlled growth of one phase, and reaction-controlled growth of the other.

In situations (1) and (2), either both phases grow in the diffusion space or one of them proves to be kinetically unstable and disappears, depending on the ratio between the fluxes of primary components through intermediate phases. Case (3) is of special interest because it allows determining the critical thickness x^*_β of the first growing phase at which the second phase emerges in the diffusion space. The authors of Ref. [10] estimated the critical thickness of Ni_2Si silicide ($x^*_\beta \sim 2$ μm) at which another equilibrium silicide, NiSi, appears.

If the intermediate compound has a small thickness, phase formation process must be a limiting one because atoms must rapidly diffuse through the thin phase interlayer. Taking into account diffusion through ultrathin layers at the initial stages, one should expect manifestation of size effects. Analysis of reactive diffusion through a very thin layer of the intermediate compound in Ref. [11] revealed violation of proportionality between the diffusion flux and the concentration gradient ($J \sim \mathrm{d}C/\mathrm{d}x$ — Fick's first law) at a layer thickness of less than 10 nm. At small thicknesses, the driving force of diffusion (gradient of concentration) markedly increases (concentration gradient $\mathrm{d}C/\mathrm{d}x \approx (C_1 - C_2)/x$, where C_1 and C_2 are the concentrations at the boundaries of the x-thick intermediate phase layer). In this case, the expression for a diffusion flux should take into account not only the linear term $\mathrm{d}C/\mathrm{d}x$ but also the higher-order terms $(\mathrm{d}C/\mathrm{d}x)^3$, etc., whose contribution increases as the thickness decreases. In other words, the dependence of the flux on the concentration gradient becomes very strong (nonlinear) at a small thickness of the intermediate phase, leading to significant acceleration of mass transfer. Due to this, the growth of the intermediate phase at early annealing stages (when its thickness is small) is a reaction-governed process. As the layer thickness increases, the flux of diffusing atoms decreases; when it reaches a certain critical value [formula (3)], the transport of atoms through the intermediate phase layer (diffusion) becomes limiting and growth kinetics is governed by diffusion.

The authors of Ref. [10] pointed out a number of limitations and assumptions of the kinetic model, viz.:

(1) The energy of phase interfaces is disregarded. Formation of an intermediate compound adds one more interface, the energy of which may further increase the total energy of the system provided the thickness of the intermediate compound is small. The net result may be the appearance of an energy barrier for the formation of a new phase nucleus.

(2) The interdiffusion coefficient $\tilde{D}$ of pure components is unrelated to the time and the thickness of the intermediate compound. The crystalline structure of the intermediate compound may change significantly during its growth. First, an amorphous silicide can appear that undergoes crystallization under suitable conditions (proper thickness and temperature); its further growth promotes collective recrystallization resulting in the improvement of the crystalline structure.

(3) The formation of metastable phases, e.g. high-temperature ones, in the diffusion space is disregarded. The metastable phases may be stabilized, for example, by the small (compared with the stable phase) crystal lattice misfit parameter at the interface, impurities, internal stresses, etc.

(4) The impurities can change the reaction barrier height at the interfaces.

3. Metastable phases in the diffusion zone

3.1 Experimental observation of metastable phases in the diffusion zone

Schwarz and Johnson [12] were the first to show that interdiffusion in thin-film crystalline metal multilayer structures may give rise to the formation of amorphous intermediate phases at the interfaces between the primary components. This phenomenon is known as a solid-phase amorphization reaction (SPAR). Later on, SPAR was described in many metallic systems largely composed of layers of transition metals, with one layer consisting of a so-called 'short-range ordered' transition metal having a small number of electrons in the unfinished d-shell (e.g., Ti, Zr, Hf, etc.), and the other of a 'far-range ordered' transition metal having a larger number of electrons in the unfinished d-shell (Fe, Co, Ni, etc.). The SPAR phenomenon was discovered by Koch at al. [13]; it is also observed during the mechanical alloying of metal powders in a ball mill. In this technology, the interdiffusion is the principal mechanism of powder fusion.

Cotts and co-workers investigated SPAR in layered thin-film Ni/Zr diffusion pairs by differential scanning calorimetry [14]. The heating temperature dependence of the thermal flow rate displays two well apparent peaks of heat release corresponding to two different processes. The maximum of the first (higher and broader) peak is observed at 580 K (for an initial thickness of the Ni and Zn layers of 30 nm) and corresponds to amorphization of the primary crystalline components. Heating gives rise to the formation of an amorphous $Ni_{68}Zr_{32}$ alloy at the interface between the Ni and Zn layers; its composition corresponds to the averaged composition of the initial multilayer structure. The formation heat of the amorphous alloy amounts to 35 ± 5 kJ mol^{-1}. The second (lower and narrower) peak of heat release corresponding to crystallization of the amorphous alloy occurs at 830 K. Crystallization enthalpy is 4.2 ± 0.2 kJ mol^{-1}, i.e., approximately one order of magnitude lower than the thermal effect of SPAR, which suggests a small difference between the internal energies of amorphous and crystalline alloys having similar chemical compositions; therefore, the driving forces of the chemical reaction (see Section 3.2) yielding crystalline and amorphous compounds are similar, too. In the same study, the interdiffusion activation energy in the amorphous alloy is estimated at $Q = 1.05 \pm 0.05$ eV, with Ni atoms being the dominant diffusing species in the Ni/Zr diffusion pair [14]. For this reason, the above value of the activation energy can be attributed to the partial diffusion coefficient of Ni atoms in the amorphous $Ni_{68}Zr_{32}$ alloy.

The same authors carried out a similar study using multilayer structures consisting of foil layers [15]. Twenty-six-μm-thick Ni and Zr foils were cold-rolled together, folded, and rolled again. The folding and rolling procedure was repeated many times. The resulting multilayer structures had separate Ni and Zr layers much thicker than in the previous study [14], where the specimens were obtained by magnetron sputtering. Despite different methods of fabrication, the heat release curves depending on heating temperature were very similar. As shown in Ref. [15], amorphous alloys are characterized by a wide homogeneity region (~ 20 at.%) and the linear variation of concentration from $Ni_{68}Zr_{32}$ to $Ni_{47}Zr_{53}$. An alloy containing even more Zr forms near the interface between the amorphous phase and the pure Zr layer. It is here that the crystalline NiZr phase with the orthorhombic lattice nucleates and grows, as confirmed by cross-sectional electron microscopy [16]. The amorphous phase continues to co-exist with the growing crystalline phase during annealing. The thickness of the amorphous phase is roughly 100 nm when annealing proceeds at $T_{an} = 320\,^{\circ}$C for 8 h. Its maximum thickness at which nucleation of the crystalline phase begins is virtually independent of temperature within the range $300 \leqslant T_{an} \leqslant 360\,^{\circ}$C. The crystalline phase grows at the interface with pure zirconium, NiZr-on-Zr, but not with the amorphous alloy. According to Ref. [15], the crystallization activation energy of an NiZr amorphous alloy is $Q_c = 2.0 \pm 0.1$ eV, i.e., significantly higher than the diffusion activation energy. It is this fact that predetermines the growth of the amorphous phase at the initial stages of diffusion annealing. It was also noticed in Ref. [15] that the diffusion coefficient decreases with a rise in annealing time and amorphous alloy thickness. This observation was attributed to structural relaxation of the amorphous substance.

The authors of Ref. [17] arrived at a similar conclusion in the study of diffusion and thermal stability of the amorphous $Co_{89}Zr_{11}$ alloy, the composition of which corresponded to that of the deep eutectic in the phase diagram of the Co/Zr binary system. Amorphous samples were fabricated by hardening from the liquid state. The activation energy Q and pre-exponential factors D_0 of diffusion of radioactive isotopes ^{57}Co and ^{195}Au in the amorphous $Co_{89}Zr_{11}$ alloy were determined. The authors also attributed the decrease in the diffusion coefficient with increasing time of diffusion annealing to structural relaxation of the amorphous substance. The irreversible structural relaxation transforms the amorphous substance from a less to a more stable (but still metastable) state. As a result, the excess free volume (quasivacancies) decreases under the effect of thermal treatment, and the remaining free volume is inherent in the relaxed amorphous state. The diffusion coefficient after structural relaxation depends only on the temperature and corresponds to the quasiequilibrium (relaxed) amorphous state. Crystallization and structural relaxation of amorphous Si and Ge were

considered in the work of F Spaepen and co-workers [18, 19]. As shown in Ref. [18], amorphous Ge undergoes continuous structural relaxation up to the moment of crystallization at $T_c = 760$ K. The thermal effect of structural relaxation is estimated at 6.0 kJ mol^{-1} and constitutes an essential part of the thermal effect at crystallization (11.6 ± 0.7 kJ mol^{-1}).

Numerous experimental data indicate that amorphous silicides in Mo/Si [4, 20–22], Ti/Si [23–26], V/Si [25], Ni/Si [27], Co/Si [28], Rh/Si [29], Gd/Si [30], Tb/Si [31], and other multilayers are frequently formed at the metal/silicon interface in the initial time. The driving force of silicide (including amorphous ones) formation is the negative heat of metal/silicon mixing that was calculated for many metal/silicon pairs in Ref. [32] based on the Miedema model [33].

3.2 Models explaining the formation of metastable phases at interfaces in the initial time

Bene [34] proposed an explanation for the early formation of metastable phases at interphase boundaries, based on the principles of nonequilibrium thermodynamics. In the very beginning, the intermediate phase nucleates and grows under strongly nonequilibrium conditions in the presence of a large chemical potential gradient. Therefore, the main principle of equilibrium thermodynamics (principle of minimum free energy) is hardly applicable to these conditions. As a rule, the silicide with the highest negative formation energy (the energy per silicide or metal atom) is not actually the first to appear. On the contrary, it is a metastable phase (either amorphous or high-temperature) that usually forms and grows. The author of Ref. [34] hypothesized that nucleation and growth of the silicide phase at the initial stages are kinetically governed processes. The structure must evolve toward a decrease in the Gibbs free energy that is not necessarily minimal on the way of the thermodynamic system. The author compares the interphase boundary with crystallization of a strongly overcooled vapor (snowflake growth). For slight overcooling, the crystal must have a spherical shape since it possesses a minimal surface. Strong overcooling produces highly nonequilibrium shapes (snowflakes) that accelerate removal of the latent heat of crystallization and ensure a faster growth of the newly formed phase leading to a more rapid decrease in the free energy of the system.

The author of Ref. [34] argues that the principle of maximum reduction of free energy provides a basis for the selection and growth of the intermediate phase at the initial stages. Once the parabolic law of diffusion is fulfilled, the increase in the thickness (x) of the growing intermediate phase is given by

$$\frac{\mathrm{d}x}{\mathrm{d}t} \approx \frac{D}{2x}\,, \tag{4}$$

where D is the effective diffusion coefficient.

The free energy reduction rate can be written out as

$$-\Delta G\,\frac{\mathrm{d}x}{\mathrm{d}t} = -D\,\frac{\Delta G}{2x}\,, \tag{5}$$

where ΔG is the difference between free energies of the growing phase and the initial state of the separated components.

Thus, the preferred phase for thickness x is that for which product $D\,\Delta G$ has a maximum value. In this product, ΔG is the thermodynamic parameter, and the effective diffusion coefficient D is the kinetic parameter. In most cases, the maximum value of $D\,\Delta G$ must correspond to that of polycrystalline equilibrium alloys and polycrystalline metastable alloys (because diffusion at low annealing temperatures mostly occurs through the grain boundaries) and to that of amorphous alloys in the concentration range corresponding to the maximum negative value of ΔG. This criterion implies that the amorphous phase may prove preferable at initial stages of growth since the diffusion coefficient in the amorphous phase is higher than in the crystalline one. It confirms the hypothesis of Walser and Bene [7] about the formation of a glass membrane at the metal/silicon interface at the initial moment of interaction between the primary components. Under certain conditions (appropriate thickness and temperature), the amorphous phase undergoes crystallization because the value of $-\Delta G$ for the crystalline phase is greater than for the amorphous one.

Experimental evidences confirm the adequacy of the above selection criterion for the first growing phase. Ni atoms deposited on single-crystalline silicon at the Ni-on-Si interface in an ultrahigh vacuum make up an epitaxial layer of nickel disilicide, $NiSi_2$. This silicide forms owing to the small lattice mismatch between $NiSi_2$ and single-crystalline Si. The low energy of the coherent interphase boundary ensures selection of this silicide as the first nucleating phase in an Ni/Si binary system. However, a further increase in the thickness of the deposited nickel triggers the growth of the polycrystalline silicide Ni_2Si because its diffusion penetrability is higher than that of the single-crystalline layer of $NiSi_2$ disilicide.

Gösele and Tu [35] used Bene's idea [34] to modify their kinetic theory of phase selection in the diffusion zone [10] for the metastable amorphous phase. These authors considered the case when the amorphous phase has already formed and grows in the diffusion zone. They focused on the problem of critical thickness of the amorphous phase and its behavior after such thickness is reached, namely whether it will co-exist with the crystalline phase or will become kinetically unstable and disappear. To this effect, the authors estimated mutual positions of concentration dependences of Gibbs free energies for amorphous (G_a) and crystalline (G_c) phases. They found that if G_a lies below the common tangent to the dependence of the free energy of the emerging second crystalline phase (G_c) and one of the pure components, the amorphous phase can co-exist with the new crystalline phase and continue to grow. In the opposite case, when curve G_a is above the common tangent to curve G_c and one of the pure components, the amorphous phase disappears after the critical thickness is reached. In the latter case, the critical thickness is calculated using the Bene idea of the principle of maximum reduction of free energy of the system. In this case, the amorphous phase grows as long as the rate of free energy reduction is higher than in the growing crystalline phase:

$$-\frac{\mathrm{d}\Delta G_a}{\mathrm{d}t} > -\frac{\mathrm{d}\Delta G_c}{\mathrm{d}t}\,. \tag{6}$$

This ratio defines the critical thickness of the amorphous phase at which it becomes unstable with respect to the crystalline phase with a close chemical composition.

In the case of one-dimensional growth of the intermediate phase in the diffusion space (the case of layered diffusion pairs), the rate of Gibbs free energy variation can be written as

$$-\frac{\mathrm{d}\Delta G}{\mathrm{d}t} = -\frac{\mathrm{d}\Delta G}{\mathrm{d}x}\,\frac{\mathrm{d}x}{\mathrm{d}t}\,, \tag{7}$$

where $-\mathrm{d}\Delta G/\mathrm{d}x = F$ is the thermodynamic driving force (per unit area) of the solid-phase reaction at the interphase

boundary, and dx/dt is the growth rate of the intermediate phase.

As shown in experiments [14, 15, 18, 19], the thermal effect in the crystallization of an amorphous substance is small, i.e., the thermodynamic driving forces for the growth of amorphous and crystalline phases with close chemical compositions differ only insignificantly. Then, it follows from relation (7) that the growth of the amorphous phase in the diffusion space prevails if its growth rate is higher than that of the crystalline phase. An obvious case, when the growth rate of the amorphous phase may be higher than that of the crystalline one, is the nucleation of a new phase at the interphase boundary. The difficulty of nucleation of the crystalline phase, i.e., a higher energy barrier for its formation than for the amorphous phase, can be a key selection criterion for the latter at initial growth stages. Experimental validation of the Gösele and Tu theory [35] of the possible coexistence of amorphous and crystalline phases in the diffusion space was described in the preceding section with the example of the binary Ni/Zr system [16].

The authors of Ref. [29] undertook a more detailed study of conditions for the existence of the amorphous phase in the diffusion zone. Amorphous intermetallides are usually obtained by the rapid cooling of melts having a desired chemical composition. Amorphous metastable alloys are formed in the diffusion zone under constant temperature and pressure. Figure 2 presents a schematic of two kinetic paths of the solid-phase reaction in a two-layer A/B film, resulting in the formation of stable crystalline $A_\gamma B$ phase and metastable amorphous α-AB phase [29]. The dashed line shows the reaction path with a kinetic barrier Q_1 (per atom) and an energy change ΔG_1 (per atom) when an amorphous chemical compound is formed from pure components, i.e., formation energy. The solid curve indicates the path leading to the stable (equilibrium) crystalline phase with a kinetic barrier Q_0 (per atom) and a formation energy ΔG_0 (per atom). ΔG_0 is higher than ΔG_1 but the difference between the formation energies of crystalline and amorphous phases having close compositions is insignificant. Q_0 and Q_1 quantities define activation energy barriers for the formation of critical nuclei of stable crystalline and amorphous phases, respectively, at the interphase boundary between pure components. According to the classical nucleation theory,

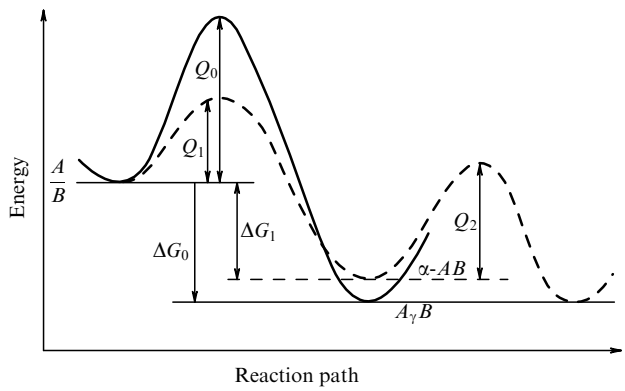

Figure 2. Schematic diagram of two kinetic paths of the solid-phase reaction in a two-layer A/B film, resulting in the formation of a stable crystalline phase $A_\gamma B$ or metastable amorphous phase α-AB [43]. Solid curve indicates the reaction path directly to the stable phase, and dashed line initially leads to the metastable phase.

the ratio between nucleation rates (N_0/N_1) of crystalline and amorphous phases is given by the relation

$$\frac{N_0}{N_1} = \exp\left(-\frac{Q_0 - Q_1}{kT}\right). \tag{8}$$

The activation energy barriers can be expressed through specific formation energies (ΔG_0 and ΔG_1) and mean specific surface energies (σ_0 and σ_1) of stable and amorphous phases, respectively:

$$Q_i = \frac{A_i \sigma_i^3}{\Delta G_i^2}, \tag{9}$$

where $i = 0$, 1 and coefficients A_i depend on the nucleus shape.

As mentioned above, the formation heat of the amorphous NiZr alloy resulting from the solid-phase reaction during annealing of a multilayer Ni/Zr film is 35 kJ mol^{-1}, and the crystallization heat of this alloy, i.e., $\Delta G_0 - \Delta G_1$, is only 4.2 kJ mol^{-1} [14]. The formation activation energy of amorphous NiZr silicide (Q_1) during solid-phase amorphization ranges 1.0–1.4 eV [14], and the crystallization activation energy of amorphous alloy (Q_2) in a wide concentration range varies between 2.5 and 5 eV [15, 29].

It follows from expression (9) that at a small value of $\Delta G_0 - \Delta G_1$, the formation activation energy of a crystalline silicide is higher than that of an amorphous one, $Q_0 > Q_1$, providing $\sigma_0 > \sigma_1$, and the precipitate shape is virtually identical. Under this conditions, the formation rate of the amorphous phase is higher than that of the equilibrium crystalline one. For small crystallization heat, the role of the thermodynamic driving force in the phase formation process (formation energy of a crystalline or amorphous alloy) is less important and the solid-phase reaction is under kinetic control. Then, the metastable phase is the preferred one due to the lower activation energy of its formation. This is considered to be the basic condition for solid-phase amorphization.

The authors argue that Bene's principle of maximum reduction of free energy (6) constitutes the mathematical (thermodynamic) condition for amorphous phase stability [34]. At the initial growth stages of the metastable amorphous phase, this condition is provided by a lower surface energy of interfaces and a higher interdiffusion coefficient D. The metastable phase is steady and continues to grow till the emerging grains of the crystalline phase form a continuous layer. For the crystalline intermediate phase to form, high mobility of both components (long-range diffusion) is needed. In contrast, the amorphous intermediate phase is formed when one component is highly mobile, while the other represents a low-mobile component (short-range diffusion). Under these conditions, the intermediate phase grows only on one of the interfaces between this phase and a pure component. One (more mobile) of the primary components is transferred across the layer of the intermediate compound toward the opposite interphase boundary where a solid-phase chemical reaction occurs to produce an amorphous alloy. The other component participates in the formation of an amorphous compound only via a series of short-range movements over the interphase boundary; it proves sufficient for the necessary short-range order to be established. Indeed, the partial diffusion coefficients of silicon and metal are significantly different in the case of silicides. In certain metal/silicon pairs (Cr, Mo, W, V, Nb, Ta with Si), the

dominant diffusing substance is constituted by Si atoms, whereas in others (Ni, Co with Si) it is metal atoms; in Pd with Si, atoms of both types have a close mobility [5]. Evidently, a higher mobility of one component in comparison with the other is an indispensable condition for the formation of the amorphous intermediate phase. As a rule, amorphous phases in many binary systems (Zr/Ni, Ti/Si, Mo/Si) are formed at moderate annealing temperatures but need higher temperatures to be crystallized.

Based on the above theoretical models and experimental data, the following scenario of events at the metal/silicon interface can be exemplified for a particular case of low annealing temperatures and amorphous silicon. These conditions are met in the low-temperature annealing of *Me*/Si multilayer structures fabricated by magnetron sputtering. The negative mixing heat of metal and silicon atoms provides the driving force for the atomic intermixing process and phase formation at the interphase boundary. There is a large chemical potential gradient at the interphase boundary between primary components at the very beginning of phase formation; therefore, the associated processes should be regarded from the standpoint of nonequilibrium thermodynamics. First, one of the amorphous silicides forms at the interphase boundary. Mass transfer across the thin amorphous phase is rather fast owing to nonlinear diffusion effects and the excess free volume of the amorphous silicide. The chemical potential gradient decreases with increasing amorphous phase thickness, and the amorphous silicide undergoes structural relaxation. Due to this, the diffusion flow declines and the silicide growth obeys a parabolic law. Crystallization occurs at a certain critical thickness of the amorphous silicide. The crystallization process may be extended in time, which accounts for the co-existence of amorphous and crystalline phases of a close chemical composition in the silicide layer.

4. The structure and X-ray optical properties of metal/silicon multilayer coatings

The above principles and models of intermediate phase nucleation and growth can be conveniently illustrated by the example of Mo/Si multilayer systems, the real structures of which have been investigated in numerous experimental studies. The possibility of practical application of periodic Mo/Si multilayer coatings in X-ray lithography gave impetus to their survey at different technical deposition parameters. Mo/Si PMCs are fabricated by several methods, viz. magnetron sputtering [4, 20, 36–38], ion-beam sputtering [39, 40], electron-beam deposition [22, 41–43], and electron-beam deposition with subsequent ion polishing of the layers [44–46]. It was revealed for the first time in Ref. [20] that Mo/Si PMCs prepared by magnetron sputtering contain amorphous intermixed zones (AIZs) between crystalline textured Mo and amorphous Si layers. In multilayer structures optimized for the operating wavelength 13.4 nm, the layer thickness is 1/4 wavelength, i.e. ca. 3.3 nm. The AIZ thickness at the Mo-on-Si interface is h(Mo-on-Si) $= 1.7 \pm 0.3$ nm. At the opposite Si-on-Mo interface, it is smaller: h(Si-on-Mo) $= 1.0 \pm 0.3$ nm. The different thicknesses of AIZs at the opposite interfaces (the so-called AIZ thickness asymmetry) was confirmed in numerous studies [4, 21, 22, 40, 47–49]. It was attributed to the large moment of Mo atoms during magnetron sputtering. Boercker and Morgan [50] used the molecular dynamics method to show that for Mo and Si atomic beams with an energy of 1 eV, stronger intermixing occurs at the Mo-on-Si interface, in contrast to a less strong atomic intermixing at the opposite Si-on-Mo interface. The strong intermixing at the Mo-on-Si interface is due to the presence of voids in amorphous silicon. However, it was shown in Refs [22, 37, 41] that AIZ thickness asymmetry also manifests itself in Mo/Si multilayer structures obtained by electron-beam evaporation. In this method, the energy of Mo atoms arriving at the substrate (0.1 eV) is essentially lower (by several electron-volts) than in magnetron sputtering. This means that the phenomenon of AIZ thickness asymmetry in Mo/Si multilayer structures is in all probability an intrinsic property of these PMCs. Also, it was demonstrated in papers [37, 41] that the AIZ growth activation energy at the Mo-on-Si interface is low (~ 0.2 eV). Although the accuracy of measuring activation energy was not very high, the order of magnitude of its value suggests that the early stages of AIZ growth at this interface are governed by surface rather than bulk diffusion.

A thin molybdenum layer is amorphous; however, molybdenum crystallizes within a narrow thickness range of $\sim 0.1-0.2$ nm after it becomes ~ 2 nm thick. A further increase in the Mo layer thickness gives rise to collective recrystallization of Mo grains. As a result, the molybdenum layer becomes textured with the texture axis [110] perpendicular to the layers of the multilayer structure. The size of the Mo grains in the growth direction is equal to the Mo layer thickness; it is severalfold greater in the lateral direction. Transition of molybdenum from amorphous to crystalline state is accompanied by a substantial decrease (1.5–2-fold) in the AIZ thickness at Si-on-Mn interfaces and a simultaneous increase of interphase roughnesses at these boundaries.

The mean chemical composition of AIZs was more difficult to determine than the thickness of amorphous intermixed zones at interphase boundaries. The formation of Mo-on-Si interfaces during deposition of Mo atoms on atomically pure Si(100) (2×1) and Si(111) (7×7) surfaces in an ultrahigh vacuum was studied in Ref. [51] by the electron diffraction method, and Auger electron and X-ray photoelectron spectroscopies. The formation of 0.4-nm-thick amorphous molybdenum disilicide $MoSi_2$ was observed at substrate temperatures of $50 \leqslant T_s \leqslant 200\,^{\circ}C$. Silicide becomes enriched in Mo as the thickness of the deposited Mo layer increases and gradually transforms into a pure Mo layer. Tunneling microscopy was employed in Ref. [52] to study the interaction of submonolayer Mo with the atomically pure Si(100) (2×1) surface. At deposition temperatures below $500\,^{\circ}C$ and further down to room temperature, Mo atoms proved to be embedded into the subsurface Si layer, where they promoted the rupture of covalent bonds and liberation of Si atoms. The free Si atoms diffused over the surface of single-crystalline silicon and congregated into islands of atomic thickness, the density of which increased with decreasing substrate temperature. Evidently, free Si atoms play an important role in the formation of AIZ at the Mo-on-Si interface at the very early stages of its appearance. Also, they contribute to the low activation energy of the AIZ formation. At a higher temperature of the single-crystalline Si substrate ($640\,^{\circ}C$), crystalline hexagonal Mo disilicide ($MoSi_2$) is formed; a further rise in the substrate temperature to $770\,^{\circ}C$ yields tetragonal Mo disilicide ($MoSi_2$) [53]. Just one to four Mo monolayers are enough for nucleation of crystalline Mo disilicide at these temperatures.

The strong asymmetry of AIZ thickness is a distinctive feature of Mo/Si PMCs. Symmetrical or weakly asymmetrical

AIZs are characteristic of other metal/silicon PMCs, such as Ti/Si [24], Rh/Si [49], and Tb/Si [31].

The technological characteristics of deposition substantially influence the PMC structure (interphase roughness, layer density and planarity, AIZ thickness at interfaces, crystalline perfection of metal layers). Substrate temperature during electron-beam evaporation, working gas pressure, distance between the substrate and the target, and substrate bias potential during magnetron sputtering are the technological parameters that determine the mobility of adsorbed atoms and thereby the conditions for the growth of individual layers of a multilayer structure. The effect of substrate temperature on the structure of Mo/Si PMC was investigated in Refs [22, 37, 41, 43]. At low substrate temperatures, the interphase roughness evolves at interfaces, which builds up from the substrate to the surface of the multilayer structure. The source of roughness is the surface of the crystalline molybdenum layer. The silicon layer does not smooth the roughness on the Mo layer surface due to the low mobility of adsorbed Si atoms; on the contrary, it inherits roughness. Taken together, the shading effect and low mobility of the adsorbed atoms promote a further building up of the interphase roughness and ensure column growth of the multilayer structure. The mobility of adsorbed atoms increases and the planarity of PMC layers improves with substrate temperature. Its rise to $T_s > 300\,^\circ$C leads to substantial thickening of AIZ on the Mo-on-Si interface, which causes deterioration of the optical properties of Mo/Si multilayer X-ray mirrors (MXMs). According to Stearns et al. [41], the optimal substrate temperature is $T_s \sim 250\,^\circ$C. At this temperature, the mobility of adsorbed atoms proves sufficient for the formation of smooth layers, while diffusion intermixing between the primary components is still insignificant.

It was shown in Refs [37, 43, 54] that a rise in working gas pressure is accompanied by the development of interphase roughness in Mo/Si multilayer structures. The enhancement of bias potential (U_b) to -100 V during Si layer deposition improves the planarity of the layers [54], whereas a similar enhancement during deposition of the Mo layer alone does not. The authors of Ref. [54] calculated the energy per adsorbed Mo and Si atom. In the former case, it is one order of magnitude higher due to the reflection of neutral Ar atoms from the molybdenum target. The Ar atoms are barely reflected from the silicon target and the adsorbed Si atoms do not receive additional energy from the reflected neutral atoms. A rise in the bias potential above -100 V leads to a marked increase of the AIZ thickness at the interphase boundaries. Optimal U_b values depend on the type of PMC materials, operating pressure, and PMC period. For short-period *Me*/Si structures with the period of $1.3 \leqslant H \leqslant 4$ nm, the optimal energy per adsorbed atom must be $20 \leqslant E \leqslant 70$ eV atom^{-1} [55].

Accelerated particles arriving at the growing surface induce undesirable processes of ion intermixing and widening of interphase boundaries. These processes are especially unwanted in manufacturing PMCs with ultrathin layers for example, MXMs for the water window ($\lambda = 2.4-4.4$ nm). In the case of normal X-ray incidence, the period of MXMs must be 1.2–2.2 nm, and the thickness of individual layers 0.6–1.1 nm. By choosing the proper energies of ions and their fluxes, it is possible to fabricate such short-period multilayer mirrors with minimal roughness and intermixing [56]. The authors of Ref. [57] came up with an idea of engineering interfaces by forming the first atomic layer at the interphase boundary at a low ion flux energy to prevent component intermixing at the interface. After the first atomic layer is formed, the ion beam energy may be increased to ensure the formation of a dense and smooth layer. This idea was successfully realized in manufacturing Ni/V MXMs with a period of 1.2 nm and a record-breaking reflection coefficient at the X-ray radiation energy $E = 511$ eV [58].

Mo/Si MXMs are the most promising elements for 13.5-nm X-ray lithography. The multimirror systems of an X-ray lithograph make high demands on the reflectance of each mirror. The maximum theoretical reflection coefficient of optimal normal-incidence Mo/Si MXMs at the above wavelength is $R_{th} = 75.5\,\%$. The period of such mirrors is $H = 6.92$ nm, and the thickness of the Mo layer makes up 40% of the period, i.e., $h(\mathrm{Mo}) = 2.8$ nm. The use of various techniques for deposition and introduction of diffusion barriers at interphase boundaries have made it possible to manufacture near-normal incidence MXMs with the reflection coefficient $R_{expt} = 69-70\%$ [59–62]. The employment of barriers allows it to be further increased by a few percent. Alternatively, diffusion barriers may be helpful for increasing the thermal stability of MXMs and extending their operating temperature range [63–68].

Periodic W/Si multilayer coatings are utilized as optical elements in the range of soft X-ray radiation, $1.5 \leqslant \lambda \leqslant 3.0$ nm, e.g. for the analysis of characteristic oxygen emission ($\lambda = 2.3$ nm) and as bandpass filters for hard synchrotron radiation or hard X-ray telescopes. The structure of these PMCs has been investigated in numerous studies [20, 69–75]. Tungsten belongs to the same group of elements as molybdenum, which accounts for a large degree of similarity between W/Si and Mo/Si PMCs. Like molybdenum, tungsten passes from the amorphous to the crystalline state with a rise in the layer thickness [75]. AIZs are evidenced at interphase boundaries. In a crystalline tungsten layer, the AIZs become asymmetrical.

5. Diffusion and phase formation in metal/silicon multilayer thin-film compositions

A review of data on the formation of metal silicides as exemplified by diffusion interactions in polycrystalline metallic films on single-crystalline silicon with a (111) or (100) orientation can be found in monographs [5, 6]. As a rule, films with thicknesses below 100 nm were obtained by electron-beam evaporation. The principal method for studying silicide formation kinetics and chemical composition was based on Rutherford back scattering (RBS). Its disadvantage is the difficulty in identifying the composition of phases less than 20 nm in thickness, when they are located at the Si/metal interface a few hundred nanometers below the metal surface. Three main silicide classes are distinguished in annealed structures formed by metallic films and single-crystalline silicon, viz. metal-rich Me_2Si silicides, *Me*Si monosilicides, and $Me\mathrm{Si}_2$ disilicides. The types of silicides and their formation sequence are listed in Table 1. The growth kinetics of metal-rich silicides follows the parabolic law with an activation energy of about 1.5 eV. The temperature of the formation origin for all 5 silicides is $\sim 200\,^\circ$C. The generation of monosilicides is also described by the parabolic law of growth, but its activation energy ranges from 1.6 to 2.5 eV. The formation temperature of monosilicides is higher than that of metal-rich silicides (usually above $350\,^\circ$C). The

Table 1. Formation of silicides in structures composed of metallic films and single-crystalline silicon.

Metal	Silicides		
Mg		Mg_2Si (single phase)	
Pt, Pd	Pt_2Si		PtSi (final phase)
Ni, Co	Ni_2Si	NiSi	$NiSi_2$ (final phase)
Ti, (Zr), Hf, Fe, Rh, Mn	HfSi		$HfSi_2$ (final phase)
V, Nb, Ta, Cr, Mo, W	VSi_2		

formation temperature of transition metal disilicides is close to 600 °C, and their formation energy is 1.7–3.2 eV.

In experiment, transition metal disilicides obey both parabolic and linear laws of growth. As shown in Refs [5, 6, 76], the growth kinetics essentially depends on the purity of the metal/silicon interface. The diffusion marker technique was applied to identify the dominant diffusant for a number of silicides. When metal-rich Me_2Si silicides are formed, the diffusion of deposited metal atoms prevails. For example, metal atoms in the three types of silicides (Ni_2Si, Mg_2Si, and Co_2Si) listed in Table 1 are the main diffusing component. It is supposed that metal atoms pass across the silicide layer, emerge at the silicide/silicon interface, and occupy interstitial positions in silicon; they weaken and rupture covalent bonds at low temperatures at which these silicides are usually formed. In contrast, it is the disilicide that forms first when the diffusion flow is dominated by silicon. Disilicides of high-melting metals form at rather high temperatures when the phonon energy is sufficient to break up covalent bonds and release silicon atoms. Free Si atoms diffuse through the growing silicide layer toward the *Me*-on-$MeSi_2$ interface, where the chemical reaction occurs, yielding disilicide. Silicide formation in a diffusion pair of Mo film (80 nm)/single-crystalline silicon (111) was studied in Ref. [77] by the RBS method. Annealing in a temperature range of 475–550 °C resulted in the growth of hexagonal molybdenum disilicide, $MoSi_2$, with an activation energy of 2.4 eV, in agreement with the parabolic law. Silicon diffusion also prevailed in the case of monosilicides.

The use of high-resolution cross-sectional TEM enabled the authors of Ref. [78] to observe phase formation at interphase boundaries at the atomic level. An in-depth study of silicide formation in Mo/Si PMC with the period $H = 13.0$ nm under conditions of pulsed annealing or *in situ* annealing in the column of a high-resolution electron microscope is reported in Ref. [4]. AIZ thickness at Mo-on-Si and Si-on-Mo interfaces in the primary PMCs was h(Mo-on-Si) = 1.9 nm and h(Si-on-Mo) = 1.1 nm, respectively. Fast thermal annealing at 400 °C for 30 s affected neither the PMC microstructure nor the thickness of either AIZ. After annealing at 450 °C for 30 s, both of AIZs widened to h(Mo-on-Si)= 2.4 nm and h(Si-on-Mo) = 1.4 nm. Either AIZs displayed atomic planes, suggesting the onset of silicide crystallization. The microdiffraction pattern of this sample obtained in the foreground with the aim of increasing the irradiated PMC volume showed three lines attributable to hexagonal molybdenum disilicide h-$MoSi_2$. It grew at the Mo-on-Si interface to the thickness h(Mo-on-Si) = 6.5 nm after annealing at 500 °C for 30 s. The thickness of the other AIZ at the opposite Si-on-Mo interface remained virtually unaltered. *In situ* annealing at $T_{an} = 275$ °C for 75 min resulted in an increase in AIZ thickness at the Si-on-Mo interface to h(Si-on-Mo) = 1.5 nm and partial AIZ crystallization. The AIZ at the Mo-on-Si interface did not crystallize till the temperature rose to 375 °C. Crystallization of this AIZ became apparent after annealing at 385 °C for 45 min. The microstructures of samples annealed *in situ* at 385 °C for 45 min and after pulsed annealing at 450 °C for 30 s looked similar in micrographs. The activation energy was estimated at 2.0 eV from the decrease in the period of the multilayer structure after pulsed annealing in a temperature range of 400–500 °C. A similar value (2.3 eV) was obtained in Ref. [79], where cross-sectional TEM was employed to study the growth of h-$MoSi_2$ on single-crystalline silicon in the temperature range from 560 to 580 °C. Moreover, the authors determined pre-exponential factor D_0 in the expression for the diffusion coefficient as equaling 14 $cm^2\,s^{-1}$.

The authors of Ref. [80] also used cross-sectional TEM to study thermal stability of Mo/Si MXMs with the period $H \sim 7.0$ nm at the relatively low temperatures of 250–350 °C. AIZ thickness was measured directly from TEM images. Isothermal annealing revealed two stages in the increase in AIZ thickness. One (fast) was followed after a certain time (AIZ thickness) by a slow stage of increasing AIZ thickness according to the parabolic law. Whatever the annealing temperature, the AIZ growth rate at the Mo-on-Si interface was significantly higher than at the opposite Si-on-Mo interface. The authors estimated the activation energy $Q \sim 2.4$ eV and pre-exponential factor $D_0 \sim 0.005\,m^2\,s^{-1}$ for the second stage of AIZ growth at the Mo-on-Si interface. These values are in excellent agreement with the data obtained in other studies using Mo/Si PMCs [4, 48] and bilayer Mo film/single-crystalline Si coatings [77, 79, 81]. The authors of Ref. [80] plotted their own and available literature data on Mo disilicide growth kinetics in Mo/Si PMCs and bilayer Mo film/single-crystalline Si coatings in one Arrhenius graph and obtained the values of activation energy $Q \sim 2.5$ eV and pre-exponential factor $D_0 \sim 0.01\,m^2\,s^{-1}$ for the diffusion of Si atoms across the Mo disilicide layer. In Refs [4, 48, 77, 79–81], the thickness of the growing Mo disilicide layer was measured by direct cross-sectional TEM or the RBS method.

Substantially different (much smaller) values of interdiffusion parameters in Mo/Si multilayer structures are reported in papers [82–84]. In Ref. [83], activation energy $Q = 105$ kJ $mol^{-1} \approx 1.1$ eV and pre-exponential factor $D_0 = 2 \times 10^{-16}\,m^2\,s^{-1}$. In two other papers [82, 84], the activation energy is even lower, 73 kJ mol^{-1} and 0.37 eV, respectively. In these studies, the parameters of interdiffusion were calculated from the relative decrease in the first-order reflection intensity in the small-angle X-ray diffraction spectrum during annealing of short-period PMCs. The theory behind this method for the determination of the diffusion coefficient was expounded in a study by Cook and Hilliard [85]. The method has been widely used to determine interdiffusion coefficients in binary systems. Its principal formula linking the relative decrease in the first Bragg peak with the interdiffusion coefficient was derived on the assumption that the primary components are fairly well intermixed and the concentration profile is described by a sinusoid; also, the small-angle X-ray profile must exhibit a

single (first) Bragg peak. However, the small-angle X-ray spectra from Mo/Si PMC presented in Refs [82, 83] display several Bragg peaks, suggesting that the concentration profile is more complicated than the sinusoidal one. It may be a source of errors in estimation of diffusion coefficients, and hence of activation energy and the pre-exponential factor. Evidently, this method is hardly applicable to binary systems with poor mutual solubility of the constituent components and intermediate phases between pure components. It is these features that are intrinsic in transition metal/silicon binary systems.

In periodic Ti/Si multilayer coatings, unlike Mo/Si PMCs, amorphous intermixed zones grow at the opposite interphase boundaries with similar rates and do not undergo crystallization at short-time (30-s) pulsed annealing up to 450 °C [24]. The composition of AIZs corresponds to that of $TiSi_2$ disilicide. Diffusion-governed disilicide formation has activation energy $Q \sim 2.0$ eV and pre-exponential factor $D_0 \sim 2.4$ cm^2 s^{-1}. Silicon atoms are the dominant diffusants in this diffusion pair.

At the initial stages of low-temperature phase formation, a silicide remains amorphous until it reaches a certain threshold thickness. During isothermal annealing, it undergoes a series of events, including diffusion of atoms of the primary components through the silicide layer, viscous flow, and relaxation of the excess free volume of the amorphous solid [86]. The free volume model of the amorphous solid was proposed by Cohen and Turnbull [87, 88] and further developed by Spaepen [89]. In this model, the free volume v_f (per mean atomic volume Ω) of an amorphous solid body obtained by rapid cooling from the liquid state or vacuum deposition is much greater than the equilibrium free volume v_f^{eq} (per Ω). Annealing at a temperature below the crystallization temperature results in annihilation of the excess free volume due to structural relaxation of the amorphous solid. By analogy with crystalline solids, mass transfer in amorphous solids is considered to be a result of defect formation and motion. Viscous flow of an amorphous solid is effected by the same defects as confirmed by close activation energies of diffusion and viscous flow [86]. The concentration of defects in amorphous substance, c_f, related to its free volume v_f is given by the expression

$$c_f = \exp\left(-\frac{\gamma v^*}{v_f}\right), \tag{10}$$

where γ is a geometric factor of order unity, and v^* is the critical free volume (per Ω) necessary for a diffusion jump.

For liquids, the relationship between coefficients of diffusion D and viscosity η is defined by the Stokes–Einstein formula

$$D\eta = \frac{1}{3\pi l} k_B T, \tag{11}$$

where l is the length on the order of the atomic diameter, and k_B is the Boltzmann constant.

An analogous relation holds for an amorphous solid [86, 89]:

$$D\eta = p k_B T, \tag{12}$$

where $p = \gamma \lambda_d^2 k_{d,0}/\Omega k_{f,0}$, γ is the geometric factor, λ_d is the nearest interatomic distance, $k_{d,0}$ and $k_{f,0}$ are the number of attempts in expressions for the frequency of defect jumps needed to maintain diffusion and viscous flow, and Ω is the mean atomic volume.

For low-temperature isothermal annealing, the viscosity of an amorphous substance grows linearly with diffusion annealing time under the effect of structural relaxation [89]:

$$\eta(t) = \eta(t=0) + \frac{d\eta(t)}{dt}\, t. \tag{13}$$

The quantity $d\eta(t)/dt$ is unrelated to the isothermal annealing time.

According to formula (12), the inverse diffusion coefficient must change linearly with diffusion annealing time:

$$D^{-1}(t) = D^{-1}(t=0) + \frac{d[D^{-1}(t)]}{dt}\, t. \tag{14}$$

Independent experiments designed to determine viscosity and interdiffusion coefficients have demonstrated that quantity p in expression (12) is two orders of magnitude greater than $1/3\pi l$ in expression (11). This means that the diffusion rate exceeds the structural relaxation rate; in other words, the viscous flow of an amorphous substance requires many more jumps to occur than does diffusional mass transfer [86, 89]. Since the activation energies of diffusion and viscous flow in a relaxed amorphous substance are similar, it is supposed that $k_{d,0}$ is significantly higher than $k_{f,0}$.

The atomistic interpretation of defects in the amorphous $Pd_{52}Ni_{32}P_{16}$ alloy before and after annealing was proposed in work [90]. Atomic configurations were calculated from the experimentally found radial distribution functions. The initial and annealed states differ in the number of relatively large cavities. The number of large cavities (surrounded by tens of atoms or more) decreases as a result of structural relaxation during annealing, while the number of small ones (surrounded by nine or fewer atoms) increases. The large cavities exhibit some analogy to vacancies in crystals, even if they are strongly anisotropic in shape. The authors conclude that the larger cavities are responsible for atomic mobility (diffusion and viscous flow) and their volume is the excess free volume in the Cohen and Turnbull model [87, 88].

6. Methods of the fabrication and study of multilayer systems

6.1 Fabrication of multilayers

The author of this review prepared multilayer coatings by DC magnetron sputtering [91], which allowed obtaining the most perfect X-ray mirrors for different wavelength ranges of electromagnetic radiation. The method makes it possible to grow layered systems with very smooth interfaces, which is essential for studying interphase interactions, especially at the initial stages. Moreover, the substrate temperature remains low (40–50 °C) during sample fabrication; this fact is of importance for metal/silicon systems that start to interact even at weak heating. When using the magnetron sputtering technique, it is necessary to distinguish between several types of particles deposited onto the substrate. The growing surface is reached by sputtered atoms of the target and neutral atoms of the inert gas originating from ion charge exchange and the reflection of neutral gas atoms from the target. If the bias potential U_b is applied, the growing surface is also bombarded by inert gas ions extracted from the magnetron plasma.

All these particles have different energies. The sputtered target atoms have an energy of several electron-volts [57, 92]. That of reflected neutral atoms is determined by magnetron source voltage and critically depends on the ratio of atomic

masses of the sputtering gas and the target. Neutral inert atoms are hardly reflected from targets with atomic numbers lower than in the inert gas. The energy of inert gas ions is a function of the plasma potential (a few electron-volts) and substrate bias potential. The resulting particle energy at the substrate surface strongly depends on the product of the sputtering gas working pressure (P_{Ar}) multiplied by the target-to-substrate distance L [55, 93]. In our experiments, the product $LP_{\mathrm{Ar}} \approx 15$ Pa mm; at such a value, the loss in energy of reflected neutral atoms is negligible. In Ref. [92], the mean energy of argon atoms reflected from an Mo target was estimated at 39.3 eV. In this study, conditions of Mo deposition (working pressure $P = 0.33$ Pa, and magnetron voltage $U = -300$ V) were similar to those in our experiments ($P = 0.3$ Pa, $U = -300$ V). The average energy is close to the shift threshold of bulk Mo atoms ($E_{\mathrm{d}} = 33$ eV) [92]. The growing film surface comprises various defects of the crystal structure, on which the threshold energy of atomic displacement is smaller [57]. Due to this, the reflected neutral atoms influence the mobility of surface atoms alone, their energy being insufficient to cause effective ionic intermixing.

In the present work, the specimens were prepared in two types of setups. The first type was designed and constructed at the Physicotechnical Laboratory, Department of Metal and Semiconductor Physics, National Technical University 'Kharkiv Polytechnical Institute'. In these setups, multilayer coatings are deposited in the following way. First, the chamber is pumped down to 1.3×10^{-4} Pa to create a high vacuum, then it is filled with argon to a pressure of $(1-3) \times 10^{-1}$ Pa. Then, magnetron sources are switched on and allowed to stabilize. Silicon and metal layers are alternately deposited onto a substrate fixed on a rotating carousel. The main metal (molybdenum, scandium, tungsten, or chrome) content in the sputtered targets was 99.95 wt.% and the Si content in the silicon target was 99.999 wt.%. The volume fraction of argon in the working gas amounted to 99.993%, and those of oxygen and nitrogen were 0.0007 and 0.005%, respectively. The mass concentration of aqueous vapors did not exceed 0.007 g m^{-3}. Si, Sc, and Mo deposition rates varied from 0.3 to 0.5 nm s^{-1}.

Part of the Mo/Si PMCs was manufactured using an industrial sputtering system (MRC-903M, Fraunhofer Institute for Applied Optics and Precision Mechanics, Jena, Germany). The initial vacuum ($\sim 10^{-5}$ Pa) was created by a cryogenic pump, and a working pressure reached ~ 0.3 Pa. Mo and Si deposition rates were 0.3 and 0.5 nm s^{-1}, respectively, and the target-to-substrate distance measured 50 mm. The thickness of the Mo and Si layers was controlled by magnetron voltage and deposition time. In certain cases, a negative bias potential with respect to the ground (U_{b}) was applied to the substrate holder.

The substrates were 76-1A2Y-KEF5-380 polished silicon plates with (111) and (100) orientations, and K-12 polished glass.

6.2 Cross-sectional transmission electron microscopy

The periodicity and morphological structure of layers and interlayer boundaries were directly surveyed by the cross-sectional method, with an electron beam passing along the layers of a multilayer coating. For this purpose, cross sections of a sample were prepared by mechanical processing and ion etching [94]. TEM studies were performed with a PEM-U electron microscope (SELMI, Sumy) with ×(108,000–540,000) magnification and an accelerating voltage of 100 kV. The TEM had a line (atomic plane) resolution of 0.2 nm.

6.3 Small-angle X-ray diffraction

Small-angle X-ray reflectivity (SAXR) spectra were obtained with a DRON-3M X-ray diffractometer ($\lambda = 0.154051$ nm) in monochromatized Cu K_{α_1} radiation. Monochromatization was performed using a silicon monochromator with (110) orientation placed in front of the sample. The $\theta - 2\theta$ scanning scheme was employed.

The period (H) of PMCs was determined from angular positions of all small-angle diffraction peaks (Fig. 3) using the complete Wulf–Bragg equation and taking account of X-ray refraction [95, 96]:

$$m\lambda = 2d \sin\theta_m \left(1 - \frac{2\delta - \delta^2}{\sin^2\theta_m}\right)^{1/2}, \tag{15}$$

where θ_m is the angular position of the m-th diffraction maximum, δ is the refraction correction, m is the diffraction order number, $d(H)$ is the PMC period, and λ is the wavelength of incident radiation.

Squaring equation (15) gives

$$\sin^2\theta_m = \frac{m^2\lambda^2}{4d^2} + 2\delta - \delta^2. \tag{16}$$

Plotted in $\sin^2\theta$ vs $m^2\lambda^2/4$ coordinates, relation (16) is a straight line with slope $b = 1/d^2$ (Fig. 4). Figure 4 shows no Bragg peaks 2, 17, 20, and 23, which are virtually inapparent in the small-angle spectrum. The PMC period was calculated with the help of a linear approximation, yielding $H = 35.123 \pm 0.006$ nm. The error in period determination ($\Delta H = 0.006$ nm) was evaluated from the error Δb in determining coefficient in the linear approximation. A major contribution to the error in measuring PMC period comes from the beam deflection with respect to the goniometer axis (mismatch with exact zero position) and imperfect splitting of the X-ray beam into halves by the sample surface. With account of these experimental errors, the relative error in PMC period measurement is 0.1–0.3%.

Small-angle X-ray spectra were simulated by fitting calculated and observed spectra (the so-called direct problem). To this effect, the theoretical and experimental diffraction curves were fitted by varying the parameters of

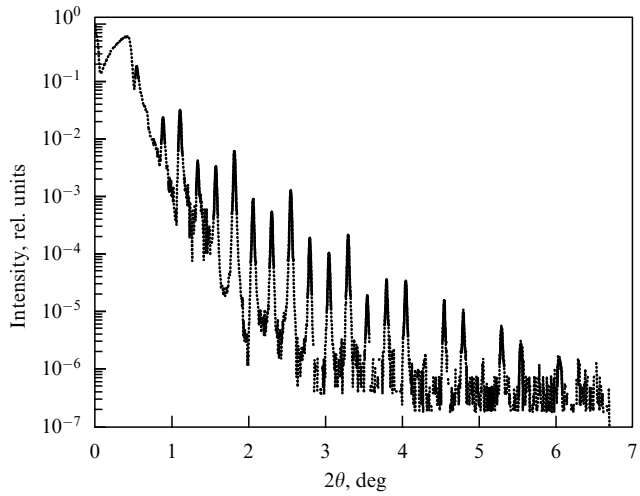

Figure 3. The small-angle X-ray spectrum of Sc/Si PMCs with the period $H = 35.12$ nm.

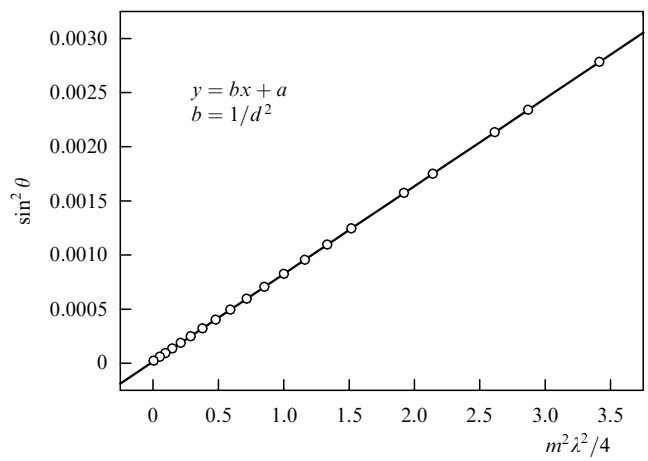

Figure 4. Dependence of $\sin^2\theta$ on $m^2\lambda^2/4$ for an Sc/Si PMC having the small-angle X-ray spectrum shown in Fig. 3.

the model structure (density and thickness of all layers, interface roughness) up to the maximum similarity of the spectra. Layer thicknesses measured from TEM images were used as the starting model parameters. The thickness values were slightly corrected in the course of simulation; simultaneously, the densities of all layers in the PMC period and interface roughness were measured.

We describe our starting and annealed multilayer structures by a three- or four-layer model. For example, each Sc/Si PMC period includes four layers: Si/ScSi/Sc/ScSi. Each interface — Si-on-ScSi, ScSi-on-Sc, Sc-on-ScSi, and ScSi-on-Si — can be described by a certain integral roughness encompassing interfacial roughness and diffuseness. For the specular reflection of X-rays, these two types of interface imperfections are virtually indistinguishable [97]. In Sc/Si PMCs, the mutual solubility of pure components (silicon in scandium, and vice verse) is either absent or insignificant. This means that geometric roughness is the main interface imperfection in the PMCs under consideration. Model diffraction spectra were calculated by the recurrence relation method [98].

6.4 Calculation of silicide thickness from the period variations in periodic multilayer coatings

The thickness of a silicide formed by annealing can be calculated from a change in the multilayer structure period. Let $\Delta h(\mathrm{Si})$, $\Delta h(Me)$ be the thicknesses of silicon and metal layers consumed to form a metal silicide of thickness $\Delta h(Me_m\mathrm{Si}_n)$. Such a chemical reaction leads to a decrease in the period:

$$\Delta h(\mathrm{Si}) + \Delta h(Me) - \Delta h(Me_m\mathrm{Si}_n) = |\Delta H|\,, \tag{17}$$

where ΔH is the difference between the periods of the annealed and initial samples.

Let us write out equation (17) in the form

$$1 - \frac{\Delta h(Me_m\mathrm{Si}_n)}{\Delta h(\mathrm{Si}) + \Delta h(Me)} = \frac{|\Delta H|\,\Delta h(Me_m\mathrm{Si}_n)}{\big(\Delta h(\mathrm{Si}) + \Delta h(Me)\big)\,\Delta h(Me_m\mathrm{Si}_n)}\,, \tag{18}$$

and introduce the shrinkage coefficient of a multilayer structure during silicide formation:

$$k = \frac{\Delta h(Me_m\mathrm{Si}_n)}{\Delta h(\mathrm{Si}) + \Delta h(Me)}\,. \tag{19}$$

Let us further write down equation (18) by introducing the shrinkage factor:

$$1 - k = \frac{|\Delta H|\,k}{\Delta h(Me_m\mathrm{Si}_n)}\,, \tag{20}$$

and express the thickness $\Delta h(Me_m\mathrm{Si}_n)$ of silicide formed by annealing through a change in the multilayer structure period ΔH and shrinkage coefficient k:

$$\Delta h(Me_m\mathrm{Si}_n) = \frac{|\Delta H|\,k}{1-k}\,. \tag{21}$$

Since the thickness of a metal silicide is known, it is possible to calculate that of silicon and metal layers consumed in the chemical reaction by the formulas

$$\Delta h(\mathrm{Si}) = n\Delta h(Me_m\mathrm{Si}_n)\,\frac{\rho(Me_m\mathrm{Si}_n)\,M(\mathrm{Si})}{\rho(\mathrm{Si})\,M(Me_m\mathrm{Si}_n)}\,, \tag{22}$$

$$\Delta h(Me) = m\Delta h(Me_m\mathrm{Si}_n)\,\frac{\rho(Me_m\mathrm{Si}_n)\,M(Me)}{\rho(Me)\,M(Me_m\mathrm{Si}_n)}\,, \tag{23}$$

where $\rho(\mathrm{Si})$, $\rho(Me)$, and $\rho(Me_m\mathrm{Si}_n)$ are silicon, metal, and metal silicide densities, respectively; $M(\mathrm{Si})$, $M(Me)$, and $M(Me_m\mathrm{Si}_n)$ are the atomic masses of silicon, metal, and silicide molecule.

The thickness ratio of metal and silicon consumed in the reaction of $Me_m\mathrm{Si}_n$ silicide formation is given by the equation

$$\frac{\Delta h(Me)}{\Delta h(\mathrm{Si})} = \frac{m\rho(\mathrm{Si})\,M(Me)}{n\rho(Me)\,M(\mathrm{Si})}\,. \tag{24}$$

By measuring from TEM images the thickness of metal and silicon consumed in the solid-phase reaction of silicide formation, it is possible to identify the type of the silicide formed by annealing at interphase boundaries.

We think that changes in the volume of periodic multilayer coatings during silicide formation occur normally to the layers. This hypothesis appears natural, since all the layers along two other directions in the plane of a PMC are rigidly coupled to each other and to the substrate.

7. Mechanism of formation of amorphous intermixed zones in Mo/Si and Sc/Si coatings

Mechanisms of formation of amorphous intermixed zones in Mo/Si PMCs are consistently explored in a series of papers [99–107]. They are essentially different for Mo-on-Si and Si-on-Mo interfaces. An AIZ at an Mo-on-Si interface arises in the process of Mo layer growth, and at the opposite Si-on-Mo interface on the already formed metal layer. It should be noted that AIZs of silicides of high-melting metals are generated at low temperatures. As a rule, the substrate temperature at which layered metal/silicon systems are formed by magnetron sputtering does not exceed 100 °C. The formation of an amorphous intermixed zone at the Mo-on-Si interface requires free Si atoms, i.e., strong covalent bonds between the atoms in the silicon layer need to be ruptured. As is known [108], single-crystalline silicon has a very high cohesion energy. At low substrate temperatures, the phonon energy is insufficient to rupture covalent bonds. Metal atoms adsorbed at the silicon layer play a key role in breaking these bonds [52]. The liberated Si atoms interact with Mo atoms arriving at the surface; jointly they form AIZs with an $MoSi_2$ composition. The growth of AIZs at this interface is limited by surface rather than bulk diffusion. The

small activation energy of Si surface diffusion (0.2 eV) facilitates Mo–Si intermixing [37, 41]. As soon as the atomic ratio of the two components amounts locally to 1:2, clusters of amorphous Mo disilicide begin to form. This silicide is adjacent to the lowest-melting eutectic in the binary Mo–Si phase diagram. A roughly 0.5-nm thick Mo layer is enough for the ≈ 1.2 nm thick AIZ to form. As the silicide layer thickness increases, the flux of Si atoms into the growing Mo layer decreases; nevertheless, part of the Si atoms penetrate into the metal layer and promote its amorphization. The growth of the metal layer is accompanied by a reduction in silicon concentration, and Mo undergoes a transition from the amorphous to crystalline state at a certain critical thickness of the layer [$h^{cr}(\text{Mo}) \sim 1.8$ nm]. The transition occurs in a narrow thickness range (tenths of nanometer). At the onset of crystallization, Mo grains are very small and the metal layer is a mixture of crystalline grains and amorphous zones (the so-called amorphous–crystalline state). After completion of crystallization and during a further increase in the thickness of the metal layer, the process of collective recrystallization proceeds effectively, with the size of Mo grains in the lateral direction being severalfold greater than the thickness of the metal layer. In the process of recrystallization, grains edged by close-packed (110) planes parallel to the layers of the multilayer structure predominantly grow. As a result, the molybdenum layers become textured and have a [110] axial texture with the axis perpendicular to the PMC layers. The axial texture does not exhibit perfection. The half-width of the rocking curve with respect to Mo (110) planes is $\sim 15°$ and remains practically constant in a range of Mo layer thicknesses from 3.3 to 10 nm. Molybdenum layers make up a solid solution of silicon atoms, the concentration of which decreases with increasing thickness of the metal layer. The metal layer has an inhomogeneous composition due to an elevated silicon concentration near the Mo-on-Si interface. AIZ thickness at this interface is ≈ 1.2 nm regardless of the structural state of the Mo layer, because the AIZ forms at the initial stage of a metal layer growth, when the layer is far from being formed. The thickness of such an AIZ is highly sensitive to substrate temperature and energy of Mo atoms adsorbed at the substrate; it grows as these parameters increase.

The AIZ at the opposite, Si-on-Mo, interface arises under quite different conditions, i.e., after the metal layer has already formed. The growth of this AIZ is limited by the diffusion of Si atoms into the near-surface region of the molybdenum layer, which remains amorphous till it reaches the thickness $h(\text{Mo}) < 1.8$ nm. The diffusion coefficient of Si atoms in the amorphous metal layer is higher than in the perfect crystalline one. The Si atoms arriving at the surface of the amorphous molybdenum layer penetrate into it as deep as ~ 0.5 nm and give rise to an AIZ of thickness $h(\text{Si-on-Mo}) \approx 1.2$ nm (Fig. 5a). The AIZ becomes a diffusion barrier hampering further penetration of Si atoms into the metal layer.

A molybdenum layer with the thickness $h(\text{Mo}) \geqslant 1.8$ nm undergoes intense recrystallization, resulting in the formation of nonequiaxial textured grains. Si atoms arriving at the metal surface penetrate into the subsurface molybdenum layer by means of bulk diffusion through a substitutional mechanism, the diffusion that is very weak in high-melting metals at such low temperatures. The net result is a thin AIZ of uniform thickness [$h(\text{Si-on-Mo}) \approx 0.6$ nm] within each Mo grain (Fig. 5b).

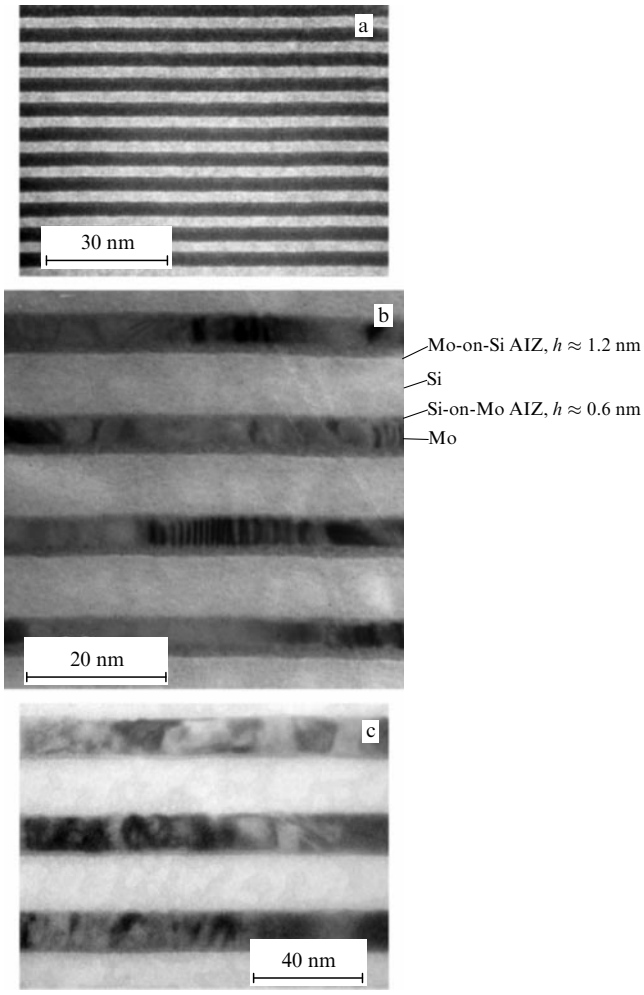

Figure 5. Cross-sectional TEM images of Mo/Si PMCs: (a) period $H = 6.12$ nm — a case of symmetrical AIZs: $h(\text{Mo-on-Si}) \approx h(\text{Si-on-Mo}) \approx 1.2$ nm; (b) period $H = 15.3$ nm — a case of asymmetrical AIZs: $h(\text{Mo-on-Si}) \approx 1.2$ nm, $h(\text{Si-on-Mo}) \approx 0.6$ nm, and (c) period $H = 34.7$ nm — a case of a single AIZ at the Mo-on-Si interface. Silicon substrate is at the bottom.

The final thickness of the amorphous intermixed zone at the Si-on-Mo interface at a given substrate temperature and atomic energy depends on the crystalline structure of the molybdenum layer. Analysis of many TEM images have shown that AIZs are not apparent at the Si-on-Mo interface when the molybdenum layer is very thick [$h(\text{Mo}) \gg 2.3$ nm]. One cause for the disappearance of this intermixed zone is compressive stress in the molybdenum layer. Compressive stress is known to reduce the number of vacancies in the metal layer, which hampers Si atom penetration (Fig. 5c).

One more (crystallographic) peculiarity of AIZ formation at the Si-on-Mo interface needs to be taken into account. As mentioned above, the layered hexagonal molybdenum disilicide ($MoSi_2$) is the first to form at low temperatures. Layers of amorphous molybdenum disilicide may inherit the perfect structure of Mo grains. Such layers may have a more homogeneous chemical composition than AIZs at the opposite interface, as follows from two facts. First, an AIZ at the Si-on-Mo interface undergoes crystallization at its small thickness and lower temperature. Second, the disilicide growth rate at this interface during isothermal annealing is significantly lower than at the opposite Mo-on-Si interface.

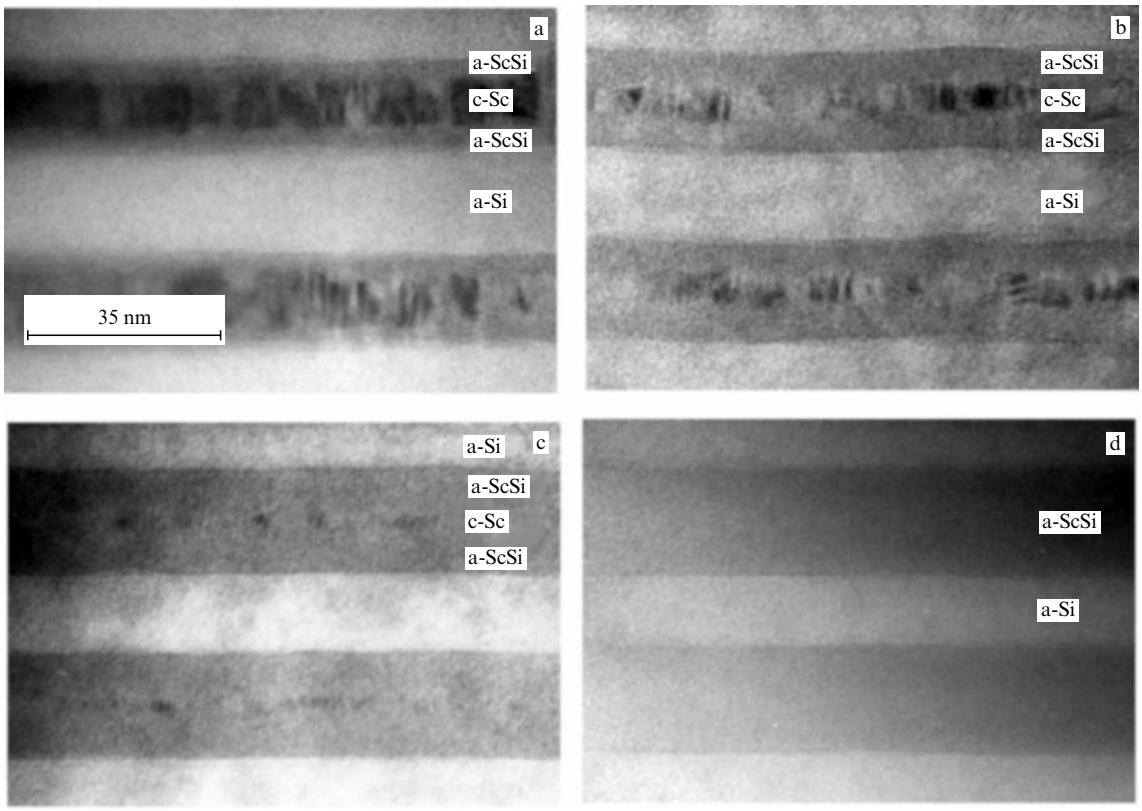

Figure 6. Cross-sectional TEM images of an Sc/Si multilayer coating before (a) and after annealing at 210 °C for 6 h (b), 24 h (c), and 41 h (d).

These features of AIZ growth are also observed in other metal/silicon multilayer coatings, including Sc/Si coatings [109–114]. AIZs at Sc-on-Si and Si-on-Sc interfaces have roughly identical thicknesses on the order of 3 nm (Fig. 6a). The diffusion barriers of W [115–120] and Cr [121] make it possible to considerably reduce the AIZ thickness in primary Sc/Si PMCs and increase their thermal stability. However, AIZ formation in Sc/Si coatings is somewhat different from that in Mo/Si PMCs. First, scandium layers are not so structurally perfect as molybdenum ones. Second, the activation energy of Si atom diffusion through scandium disilicide layers is rather low. It will be shown below that Si atoms behave as the dominant diffusing species in both pairs, Sc/Si and Mo/Si. The activation energy of Si diffusion through the silicide layer in an Sc/Si system is two times lower than in the Mo/Si system. This accounts for the very high sensitivity of AIZ thickness in Sc/Si multilayer coatings to substrate temperature.

8. Diffusion and phase transformations in Sc/Si layered systems

8.1 Kinetics of reactive diffusion in Sc/Si nanofilm coatings during isothermal annealing

The kinetics of reactive diffusion in Sc/Si film coatings during isothermal annealing have been studied in a series of papers [122–129]. Our team observed it in two types of Sc/Si samples: PMCs consisting of thin scandium and silicon layers, and three-layer coatings composed of thicker layers. The former are more convenient for the examination of the initial stages of silicide formation, while the latter are better for the study of late stages (see below). The period of the PMCs was 35 nm, and they had 20 bilayers. The thicknesses of layers in the three-layer Si/Sc/Si coating were $\sim$ 100/270/100 nm, respectively.

In order to elucidate the mechanism and kinetics of silicide formation, the samples were annealed in a vacuum of at least 10^{-3} Pa in the temperature range from 130 to 400 °C. The sample structure (first and foremost, the silicide layer thickness) was assessed after each hour of annealing by small-angle X-ray diffraction method. The results of analysis of small-angle X-ray spectra were verified by transmission electron microscopy (TEM) of randomly selected samples. The data obtained by the two methods proved to be in excellent agreement.

Figure 6a features a cross-sectional TEM image of an Sc/Si PMC in the initial state. Amorphous ScSi interlayers roughly 3 nm thick can be seen between the layers of polycrystalline scandium and amorphous silicon [114] that formed in the course of coating deposition. The thickness of amorphous alloy layers increases during heating in the temperature range from 130 to 210 °C, while the thickness of silicon and scandium layers correspondingly decreases (Fig. 6b, c) till the scandium layers are completely exhausted (Fig. 6d). The thickness of the AIZs at the opposite Sc-on-Si and Si-on-Sc interfaces is roughly equal.

Changes in the thickness of the scandium and silicon layers during annealing can be employed to estimate the mean stoichiometric composition of a growing amorphous alloy. The Sc–Si binary phase diagram shows a few silicides: Sc_5Si_3, Sc_5Si_4, ScSi, $ScSi_{1.22}-ScSi_{1.67}$ ($Sc_4Si_5-Sc_3Si_5$) [130]. The silicide containing the largest amount of silicon possesses a broad nonstoichiometric region. The known densities of different silicides are rather close: $\rho(Sc_5Si_3) = 3.299$ g cm^{-3}, $\rho(ScSi) = 3.36$ g cm^{-3}, $\rho(Sc_3Si_5) = 3.393$ g cm^{-3} [131], because

those of scandium and silicon are not themselves significantly different, either [$\rho(\mathrm{Sc}) = 3.02$ g cm^{-3}, and $\rho(\mathrm{Si}) = 2.33$ g cm^{-3}]. If the atomic weight of the primary components [$M(\mathrm{Sc}) = 45$, and $M(\mathrm{Si}) = 28.1$] is known, besides their density, it is possible to calculate the ratio of scandium and silicon thicknesses [$\Delta h(\mathrm{Sc})$ and $\Delta h(\mathrm{Si})$] consumed in a chemical reaction yielding a certain $\mathrm{Sc}_m\mathrm{Si}_n$ silicide by the formula

$$\frac{\Delta h(\mathrm{Sc})}{\Delta h(\mathrm{Si})} = \frac{m\rho(\mathrm{Si})\,M(\mathrm{Sc})}{n\rho(\mathrm{Sc})\,M(\mathrm{Si})}\,. \tag{25}$$

Formula (25) follows from formula (24).

Calculated values following from relation (25) for $\mathrm{Sc_5Si_3}$, $\mathrm{Sc_5Si_4}$, ScSi, $\mathrm{ScSi_{1.22}-ScSi_{1.67}}$ ($\mathrm{Sc_4Si_5-Sc_3Si_5}$) silicides are 2.06, 1.54, 1.24, and 0.99–0.74, respectively. It follows from a comparison of Figs 6a and 6c that 6.2 nm of Sc and 4.9 nm of Si were consumed in the reaction of silicide formation that gave rise to two silicide layers, each 4.5 nm thick. In this solid-phase reaction, scandium and silicon consumption occurred at a ratio of 1.27 : 1. Such a ratio of Sc and Si volume fractions is consistent with the reaction of ScSi silicide formation (1.24 : 1). Thus, silicide formation in Sc/Si multilayer coatings at 210 °C occurs as solid-phase amorphization giving rise to amorphous scandium silicide:

$$\text{c-Sc} + \text{a-Si} \rightarrow \text{a-ScSi}\,.$$

Figure 7 displays cross-sectional TEM images of three-layer Si/Sc/Si structures in the initial state and after annealing at 400 °C for 1 h. Obviously, reactions of silicide formation in three-layer and multilayer coatings run virtually identically. Comparison of Figs 7a and 7b shows that 54 nm of scandium reacted with 43 nm of silicon to produce 76 nm of silicide. The total thickness of silicide formed in this chemical reaction and by isothermal annealing was 79 nm. This means that scandium and silicon are consumed in the ratio of 1.26 : 1 and the silicide composition in three-layer coatings, as in multilayer ones, corresponds to ScSi stoichiometry. In other words, the silicide composition at early and late stages is similar, being independent of both silicide layer thickness and the initial thickness of the coating layers. Analysis of electron micrograph patterns showed that annealing at 400 °C for 1 h yields crystalline scandium silicide, ScSi. The same silicide is apparent in the microdiffraction pattern of the three-layer sample annealed at 350 °C for 11 h. Under these annealing conditions, the silicide has a virtually equal thickness of 79 nm, meaning that amorphous scandium silicide formed at the initial stages of annealing of three-layer structures eventually crystallizes.

Small-angle X-ray diffraction patterns of Sc/Si multilayer coatings before and after annealing at 210 °C are presented in Fig. 8. The spectrum of the primary sample exhibits ~ 25 orders of Bragg reflection from the periodic structure of a multilayer coating, with their angular position determined by Bragg's law, taking account of X-ray refraction. The number of Bragg peaks revealed in the small-angle spectra of the annealed samples remains practically the same as in the primary sample. This testifies to the fact that the amount of interphase roughness does not significantly change during annealing of the sample. The presence of a wealth of diffraction peaks in both primary and annealed samples makes it possible to calculate the coating period to the accuracy of at least 0.05 nm.

It should be emphasized that the diffraction pattern contains information on the thickness ratio of strongly and weakly scattering coating layers that determines the full set of harmonic intensities (the so-called extinction law). In the general case, this law is defined by the interference of radiation beams reflected from all interlayer boundaries of the coating. As shown in Fig. 6a, Sc/Si coatings contain four types of boundaries, viz. Si-on-ScSi, ScSi-on-Sc, Sc-on-ScSi, and ScSi-on-Si. However, the results of simulations give evidence that interface roughness at ScSi-on-Sc and Sc-on-ScSi boundaries is more pronounced than at Si-on-ScSi and ScSi-on-Si. It is ~ 1 nm at ScSi-on-Sc and Sc-on-ScSi, and twice as small (~ 0.5 nm) at Si-on-ScSi and ScSi-on-Si. Indeed, ScSi-on-Sc and Sc-on-ScSi interlayer boundaries,

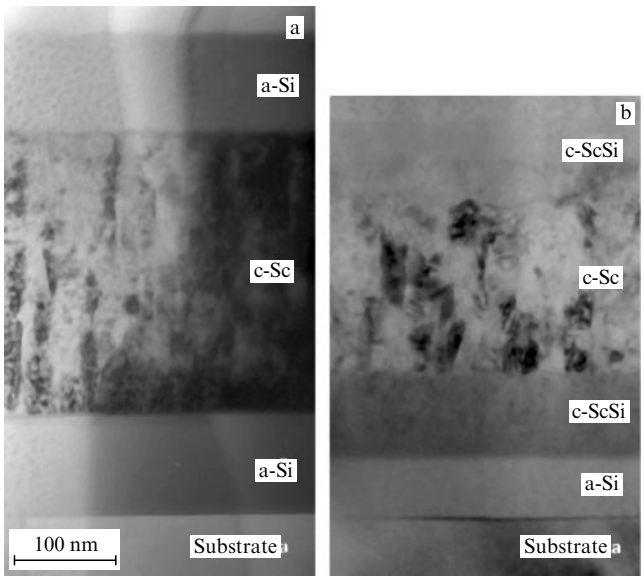

Figure 7. Cross-sectional TEM images of an Si/Sc/Si three-layer coating before (a) and after annealing at 400 °C for 1 h (b).

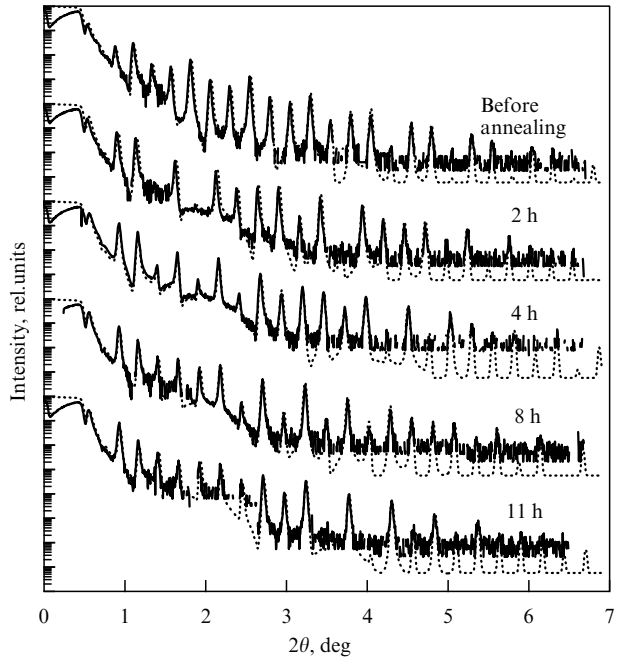

Figure 8. Small-angle X-ray diffraction patterns from an Sc/Si multilayer coating before and after annealing at 210 °C for 2, 4, 8, and 11 h. Solid lines — experiment, and dotted lines — theory.

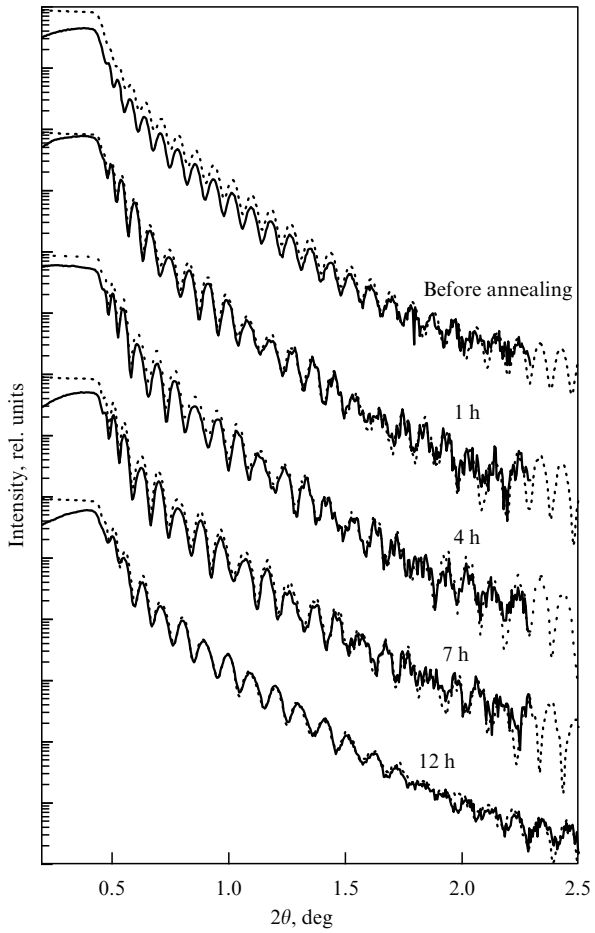

Figure 9. Small-angle X-ray diffraction patterns from an Si/Sc/Si three-layer coating before and after annealing at 300 °C for 1, 4, 7, and 12 h. Solid lines — experiment, and dotted lines — theory.

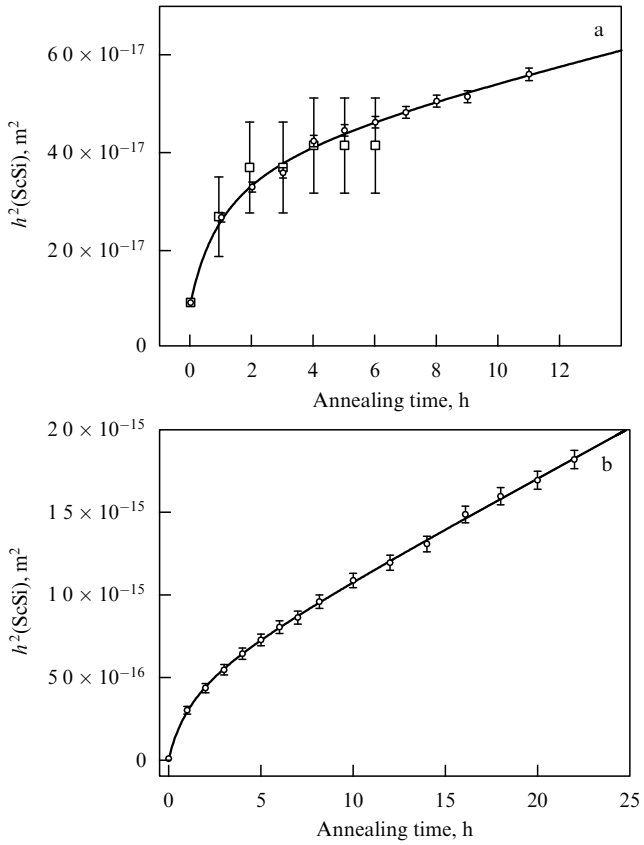

Figure 10. Dependence of ScSi silicide thickness squared on annealing time for an Sc/Si multilayer coating at annealing temperature of 210 °C (a) and for an Si/Sc/Si three-layer coating at annealing temperature of 300 °C (b). Time dependences of silicide thickness squared were approximated based on the notion of amorphous phase structural relaxation.

i.e., scandium layer boundaries, look in TEM images rougher than Si-on-ScSi and ScSi-on-Si (Fig. 6a). This is quite natural since polycrystalline scandium may actually exhibit a sufficiently high roughness in comparison to amorphous silicon and silicide layers. The contribution of rough boundaries of the scandium layer to the resulting diffraction pattern is relatively small; therefore, the extinction law is mainly determined by the position of ScSi-on-Si and Si-on-ScSi interlayer boundaries, i.e., by the thickness of the Si layer (to be precise, by the ratio of Si layer thickness to the PMC period).

The reaction of silicide formation is accompanied by a change in specific volume and, hence, in PMC period [formula (17)]. A change in the silicide thickness can be estimated from alteration of the PMC period ΔH:

$$\Delta h(\mathrm{ScSi}) = 2.09\,\Delta H\,. \tag{26}$$

This relation follows from formula (21) after the substitution of shrinkage coefficient k for ScSi silicide.

Figure 9 illustrates small-angle X-ray diffraction patterns for three-layer Si/Sc/Si coatings before and after annealing at 300 °C for 1, 4, 7, and 12 h. The character of intensity oscillations in the diffraction angle region $2\theta < 2^\circ$ is largely determined by the thickness of the upper silicon layer. This fact permits determining the thickness to the nearest ~ 0.5 nm and calculating the silicide thickness from silicon consumption by the formula

$$\frac{\Delta h(\mathrm{Si})}{\Delta h(\mathrm{ScSi})} = 0.554\,. \tag{27}$$

This relation follows from formula (22) after substitution of relevant numerical values of constants.

Figure 10a depicts the dependence of the thickness squared of amorphous ScSi silicide on the annealing time of a multilayer coating, $h^2(t)$, at an annealing temperature of 210 °C. The dependence demonstrates a rather complicated silicide growth pattern. On the one hand, the time dependence of the thickness is explicitly nonlinear ($h \sim t$), which means that the growth is at variance with boundary kinetics, i.e., unrelated to the reaction rate of silicide formation at interphase boundaries; it appears to be governed by the rate of reactant mass transfer through the silicide layer. On the other hand, the growth of the silicide does not obey a parabolic law ($h^2 \sim t$), at least at its early stages, as it does in diffusion-governed kinetics. The linear dependence $h^2 \sim t$ emerges only at very large annealing times.

It is convenient to consider the later stages of diffusion-governed interaction using three-layer coatings with thick enough layers. It should be noted, however, that silicide formation may depend on the structural perfection of metal layers, which in turn changes with their thickness. Such a dependence was observed in Mo/Si multilayer structures [99–102, 105]. In our case, the thickness of Sc layers in three-layer

structures is much greater than in multilayer systems; the structure of scandium layers is different, too. Indeed, thin scandium layers exhibit two prevalent orientations related to growth texture, (002) and (101), whereas thick scandium layers have the sole (002) orientation. The structure of scandium in three-layer samples demonstrates high perfection compared with multilayer ones as appears from the width of diffraction maxima.

For this reason, a correct comparison of the data for multilayer and three-layer samples implies the knowledge of whether the silicide growth rate is equal in these systems and whether size effects manifest themselves in them. Figure 10a illustrates the dependence of silicide growth on annealing temperature (210 °C) for the three-layer coating (squares). The lower accuracy with which the silicide layer thickness is determined from diffractograms for three-layer samples accounts for the significantly broader scatter of data points than for multilayer structures. Nevertheless, the data on three-layer and multilayer films are in excellent agreement. This means that the silicide growth rate is independent of the structure and thickness of scandium layers. Therefore, the comparison of data on three-layer and multilayer structures is quite correct.

The dependences of silicide growth rate on the time of isothermal annealing for three-layer films at 300, 350, and 400 °C are analogous to those for multilayer structures. The initial stage of nonlinear growth is followed by a well-apparent stage of growth according to the parabolic law (Fig. 10b).

The results of the present study indicate that the growth of amorphous ScSi silicide is substantially different from the classical picture. First, the growth curve in Fig. 10 lacks the section corresponding to boundary kinetics ($h \sim t$) [plotted in $h^2(t)$ coordinates this section must turn up at the end], meaning that the growth of silicide is from the very beginning (at least at a layer thickness of over 3 nm) limited by diffusion rather than a chemical reaction. In other words, the critical thickness of the intermediate phase (x_β^*) corresponding to the change in growth kinetics for the Sc/Si system is less than 3 nm.

Second, the parabolic law ($h^2 \sim t$) of growth is not fulfilled at the early stages (nonlinear time dependence of the silicide layer thickness squared). The reduced slope of $h^2(t)$ curves suggests a decrease in the effective diffusion coefficient. For example, the diffusion coefficient at 210 °C is $\sim 2\times10^{-21}\,\mathrm{m^2\,s^{-1}}$ during the first hour of annealing, $0.8\times10^{-21}\,\mathrm{m^2\,s^{-1}}$ during the second hour, and $0.3\times10^{-21}\,\mathrm{m^2\,s^{-1}}$ during the eleventh hour. At later stages, a transition to the usual reactional diffusion regime occurs and the time dependence of the layer thickness squared becomes linear. A decrease in the growth rate of an amorphous silicide was observed in the Mo/Si system [80] and in metallic glasses [17]. The possible causes for diffusion slowdown will be discussed below based on two approaches: nonlinear diffusion, and structural relaxation of amorphous layers.

Because we are dealing with atomic diffusion through ultrathin layers, it is necessary to take account of possible manifestations of size effects (see Section 2.2). At small thicknesses, the driving force of diffusion (the concentration gradient) becomes very large and enhances the atomic diffusion flux. In other words, the dependence of the flux on the concentration gradient becomes very strong (nonlinear) and results in a sharp acceleration of mass transfer. A nonlinear diffusion model must include a certain critical layer thickness characterizing transition to linear diffusion, even though it does not imply a dependence of critical thickness on annealing temperature. However, Fig. 10 shows that the layer thickness of transition to the linear stage increases with increasing temperature. The critical thickness of transition from nonlinear to linear (parabolic) diffusion can be deduced from equation (30) (see below) and Fig. 10 if the nonequilibrium diffusion coefficient D_{neq} becomes equal to the equilibrium one ($D_{\mathrm{eq}} = D_{\mathrm{par}}$). The critical thickness is 6.0, 8.6, 31.6, and 91 nm for annealing temperatures of 130, 210, 300, and 400 °C, respectively. This puts into question the adequacy of the description of silicide growth kinetics that includes size effects.

Bearing in mind the strongly nonequilibrium conditions of coating preparation (quenching from the vapor phase onto the cold substrate) and the insufficient perfection of nanocrystalline scandium layers and amorphous layers of silicon and silicide, it may be speculated that initial coatings contain a large amount of vacancy type nonequilibrium defects, excess free volume, etc. This suggests that diffusion slowdown during annealing is due to structural relaxation and annihilation of the excess free volume in the amorphous silicide layer, leading to impaired diffusion penetrability of the silicide layer. Such an approach was employed, in particular, in Ref. [86] to analyze silicide growth kinetics in an Mo/Si system. The presence of excess free volume results in the appearance of an additional term (D_{neq}) in the expression for the diffusion coefficient describing diffusion through nonequilibrium defects:

$$D = D_{\mathrm{eq}} + D_{\mathrm{neq}}\,, \tag{28}$$

$$D_{\mathrm{neq}} = \left[\frac{1}{D_{\mathrm{in}}} + t\,\frac{\mathrm{d}(1/D_{\mathrm{neq}})}{\mathrm{d}t}\right]^{-1}, \tag{29}$$

where D_{in} is the diffusion coefficient at the initial instant of time. The nonequilibrium constituent of the diffusion coefficient decreases as the annealing time increases and vanishes as the time tends to infinity. Taking account of the nonequilibrium constituent of the diffusion coefficient, the parabolic law ($h^2 = 4Dt$) of layer growth transforms into

$$h^2 = 4\left\{\left[\frac{1}{D_{\mathrm{in}}} + t\,\frac{\mathrm{d}(1/D_{\mathrm{neq}})}{\mathrm{d}t}\right]^{-1} + D_{\mathrm{eq}}\right\} t\,. \tag{30}$$

Because silicide interlayers h_0 in thickness already exist by the onset of annealing, the final expression for silicide growth rate during isothermal annealing takes the form

$$h^2 - h_0^2 = 4\left\{\left[\frac{1}{D_{\mathrm{in}}} + t\,\frac{\mathrm{d}(1/D_{\mathrm{neq}})}{\mathrm{d}t}\right]^{-1} + D_{\mathrm{eq}}\right\} t\,. \tag{31}$$

Formula (31) was used to approximate experimental data on silicide growth. The results of such approximation are presented in Fig. 10a, b (solid thin lines). Diffusion coefficients during parabolic growth (D_{eq}), and at the initial instant of time (D_{in}) (annealing time $t = 0$) were used as adjustable parameters. Arrhenius plots for D_{eq} and D_{in} are represented in Fig. 11. The diffusion activation energy for the parabolic section of growth curve is 1.0 eV, and the pre-exponential factor $D_0 = 4\times10^{-12}\,\mathrm{m^2\,s^{-1}}$.

We showed by the diffusion marker method (see Section 8.2 below) that silicon is the fast diffusant in Sc/Si systems. The inherent diffusion coefficient of silicon is 20 times that of scandium. Therefore, the above diffusion characteristics (activation energy and pre-exponential factor) describe silicon diffusion in an ScSi silicide layer.

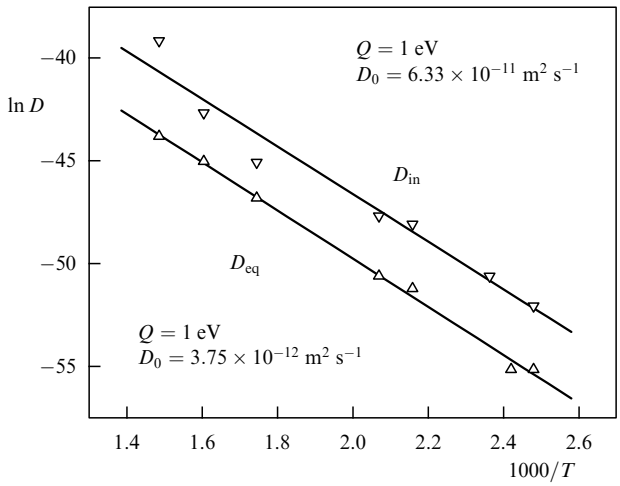

Figure 11. Arrhenius dependence for the growth of ScSi silicide at early and late stages, where the parabolic law is fulfilled.

Arrhenius plots give low values of diffusion activation energy and the pre-exponential factor ($Q = 1.0$ eV, and $D_0 = 4 \times 10^{-12}$ m^2 s^{-1}). In our experiments, scandium silicide remains amorphous in multilayer structures at all annealing times and temperatures and at the initial annealing stages for three-layer structures. Under certain annealing conditions ($T_{an} = 400\,°C$, $t_{an} \leqslant 1$ h and $T_{an} = 300\,°C$, $t_{an} \leqslant 11$ h), the silicide undergoes crystallization in three-layer specimens. We do not notice any change (within the scatter of the measurement) in the activation energy during transition from silicon diffusion in the amorphous silicide to that in the crystalline ScSi silicide. This may be attributed to two causes. First, the silicide layer at the initial stages of crystallization may be a mixture of amorphous and crystalline phases (the so-called amorphous–crystalline state). Second, annealing at low temperatures gives rise to a crystalline silicide with an imperfect structure in which diffusion through structural defects (e.g. dislocations and intergrain boundaries) plays an important role. The activation energy of diffusion through crystalline structure defects is much lower than in the bulk of a perfect crystal.

Free volume annihilation must be accompanied by narrowing of diffusion activation energy spectra in an amorphous substance and a rise in the mean effective activation energy. However, the broad scatter of experimental points in the Arrhenius plot for D_{in} does not permit us to accurately determine the activation energy at the early stages of silicide growth. On the average, the diffusion coefficient at the initial instant is 15–20 times the equilibrium diffusion coefficient, which corresponds to a rise in energy by 0.1 eV (within the measurement error of activation energy for D_{in}) due to structural relaxation.

Thus, the processes of silicide formation in Sc/Si film systems in a temperature range of 130–400 °C proceed as a solid-phase reaction

$$\text{c-Sc} + \text{a-Si} \rightarrow \text{a(c)-ScSi}\,.$$

The composition of the resulting silicide is close to ScSi. At the initial stages of growth, the scandium silicide is amorphous. It undergoes crystallization during annealing of three-layer samples (400 °C for $\leqslant 1$ h and 300 °C for $\leqslant 11$ h) at a roughly equal thickness of 79 nm. Neither its composition nor growth rate depends on the scandium and silicon layer thickness. The growth of the amorphous silicide starting from the earliest stages ($h \geqslant 3$ nm) is consistent with diffusion-governed kinetics. The section of the silicide growth curve corresponding to the reaction-governed diffusion ($h \sim t$) is absent. Diffusion of silicon atoms through the silicide layer is characterized by low values of activation energy (1.0 eV) and the pre-exponential factor $D_0 = 4 \times 10^{-12}$ m^2 s^{-1}. The early growth of the amorphous silicide is of a clearly marked nonlinear character (the parabolic law of growth $h^2 \sim t$ is not fulfilled). In the course of annealing, transition to the classical parabolic growth occurs and the diffusion coefficient decreases 15–20-fold. Silicide growth kinetics is fairly well described based on the concepts of structural relaxation and free volume annihilation in the growing silicide layer.

8.2 Detection of the dominant diffusant in the Sc/Si system by the diffusion marker technique

The dominant diffusing species in thin-film metal/silicon and metal/metal diffusion pairs are detected with the use of diffusion markers (usually thin discontinuous tungsten layers). Their displacement, caused by the Kirkendall effect, is determined by the RBS method. The Kirkendall effect shows itself as the nonconservative motion of dislocation defects in the diffusion zone allowed by excess vacancies arising from the difference between partial diffusion coefficients of constituent components [8]. This approach was successfully employed to study diffusion pairs composed of films several hundred nanometers thick or more [6]. However, the RBS method is inapplicable to nanothick Sc/Si PMCs for lack of the necessary spatial depth resolution. It does not allow registering marker displacement for a distance smaller than a few dozen nanometers (≈ 30 nm), commensurate with the PMC period. The method proposed in Ref. [6] permits determining marker shifts of less than 0.1–0.2 nm. The periodicity of layers in PMCs makes it possible to apply small-angle X-ray diffractometry for the precision measurement of marker positions. In what follows, it will be shown that a combination of small-angle X-ray diffractometry and cross-sectional TEM can be used to determine the ratio of partial diffusion coefficients at the earliest interdiffusion stages.

Diffusion markers are usually placed at the interface of a diffusion pair. However, such an approach is unsuitable for nanoscale layers, since the markers are carried away by the moving interface during annealing [6]. Separation of the markers from the interface results in an additional interphase boundary and, as a consequence, in additional energy consumption. An effective attractive force arising between the interface and the markers is responsible for their being carried away by the moving interface. Tardy and Tu [132] studied the growth of the Al_3Ti intermediate phase in a two-layer Al/Ti film structure and observed the entrainment effect of the markers during prolonged diffusion annealing. The markers could be separated from the moving interface only after the intermetallide became as thick as 500 nm. We placed diffusion markers inside the silicide layer to avoid this artefact. The following method for deposition of PMC layers with diffusion markers has been proposed.

Periodic Sc/W/Si/W multilayer compositions with W-based diffusion markers were obtained by the same procedure as Sc/Si PMCs, with the sole difference being that two approximately 0.14 nm thick tungsten layers were deposited in each period by magnetron sputtering. Their deposition rate was made low (0.025 nm s^{-1}) to ensure the

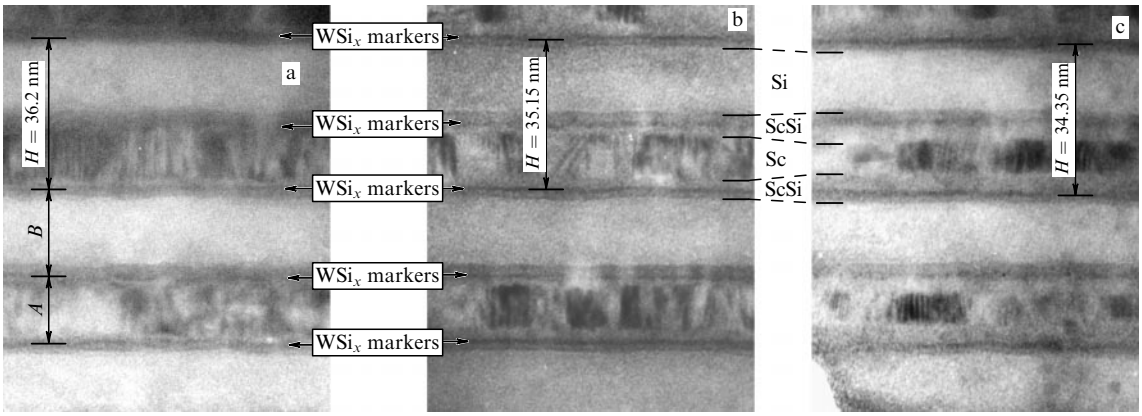

Figure 12. Cross-sectional TEM images of an Sc/W/Si/W multilayer structure with tungsten-based diffusion markers before (a) and after annealing at 230 °C for 1 h (b) and 6 h (c).

island structure of the tungsten-bearing layers. Two W-containing layers were deposited in each PMC period to separate diffusion-induced migration of the diffusion markers and movements of the Si-on-ScSi interface. Each PMC period consisted of 6 deposited layers, Sc(4.5)/W(4.5)/Sc(54.7)/W(4.5)/Sc(4.5)/Si(54.7), where the figures in parentheses indicate the deposition time (in seconds) for each layer. Thus, the first tungsten layer was deposited on the 1-nm thick Sc sublayer, and the second one was covered by an Sc sublayer of the same thickness. It will be shown below that this technological procedure gave the desired result, i.e., localization of the diffusion markers inside the silicide layers that formed in the course of preparation of the given multilayer structure. The resulting PMCs were subjected to isothermal annealing in the temperature range from 210 to 250 °C in vacuum. Their characteristics, including the period, individual layer thickness, and marker positions, were determined by the small-angle X-ray diffraction method, as described above.

Figure 12 [133] displays TEM images of periodical Sc/W/Si/W multilayer structures with diffusion markers before and after annealing at 230 °C for 1 and 6 h. These markers are easy to detect against the background of relatively light silicide layers due to the high absorption capacity of tungsten. The diffusion markers are located inside amorphous silicide layers (somewhere in the middle). This means that interphase boundaries do not attract them or that they have already been separated from the interfaces. In this way, we managed to avoid the entrainment of the markers by moving interfaces during subsequent annealing.

In isothermal annealing, amorphous scandium silicide grows largely between the diffusion markers and the scandium layer, whereas the distance between the markers and the ScSi-on-Si (Si-on-ScSi) interface does not substantially increase (Fig. 12b, c). This suggests the key role of Si atoms in mass transfer; they diffuse from the pure silicon layer through the scandium silicide layer toward the Sc-on-ScSi (ScSi-on-Sc) interface where silicide is formed. Thus, the partial diffusion coefficient of Si atoms is significantly higher than that of Sc atoms in scandium silicide.

As a consequence, distance A (see Fig. 13) between diffusion markers across the Sc layer increases, whereas distance B between the markers across the Si layer decreases. Precision measurement of A and B variations in the course of isothermal annealing makes it possible to find the ratio between partial diffusion coefficients, $R = D(\mathrm{Si})/D(\mathrm{Sc})$. Notwithstanding that TEM shows pictorially the growth of silicide, we made use of small-angle X-ray diffractometry for precision measurement of the changes in distances between A and B markers. Despite the small thickness of W layers, they strongly influence the intensity distribution in the small-angle spectrum, which makes possible precision measurement of distances between the markers by simulating such a spectrum. Changes in the thickness of the newly formed scandium monosilicide, $\Delta h(\mathrm{ScSi})$, were computed from variations of the period of the multilayer structure using formula (26), and the thicknesses of the consumed components, $\Delta h(\mathrm{Si})$ and $\Delta h(\mathrm{Sc})$, were made by formulas analogous to Eqns (22) and (23).

Calculated values of $\Delta h(\mathrm{Sc})$, $\Delta h(\mathrm{Si})$, and $\Delta h(\mathrm{ScSi})$ for diffusion annealing at 230 °C during 1, 2, 6, and 12 h are

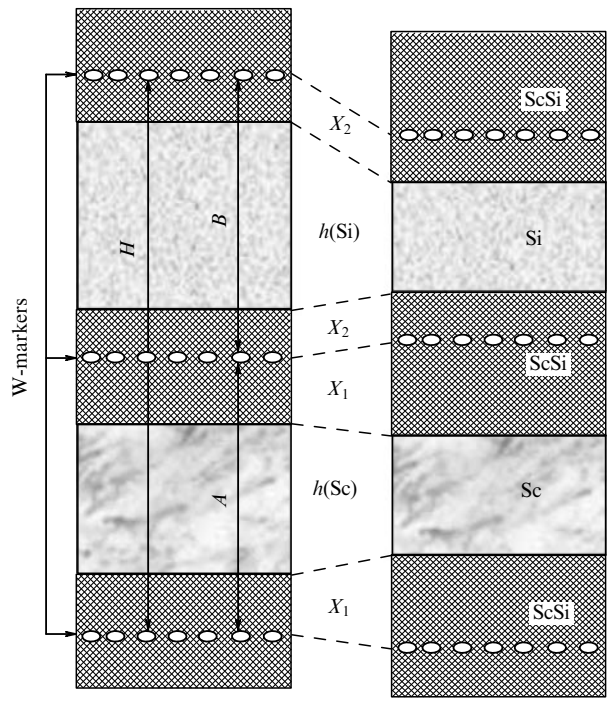

Figure 13. Schematic representation of an Sc/W/Si/W multilayer structure with diffusion markers, illustrating calculation of the ratio between partial diffusion coefficients [$R = D(\mathrm{Si})/D(\mathrm{Sc})$].

Table 2. Parameters of an Sc/W/Si/W multilayer structure before and after annealing.

Annealing time, hours ($T_{an} = 230\,°C$)	Parameters of the multilayer structure, nm									$R = D(Si)/D(Sc)$
	H	A	B	ΔH	Δh(ScSi)	Δh(Sc)	Δh(Si)	$2\Delta X_1$	$2\Delta X_2$	
0	36.2	13.2	23.0	0	0	0	0	0	0	
1	35.15	14.4	20.8	1.05	2×2.2	3.0	2.43	4.2	0.18	23
2	34.9	14.6	20.3	1.30	2×2.7	3.7	3.0	5.2	0.26	20
6	34.35	15.2	19.15	1.85	2×3.9	5.3	4.3	7.3	0.38	19.1
16	33.6	16.1	17.5	2.6	2×5.4	7.4	6.0	10.3	0.52	19.9

presented in Table 2. By way of example, the period of the multilayer structure decreased by 1.05 nm after annealing for 1 hour. This means that the thickness of each silicide layer increased by 2.2 nm, while the thickness of the Sc and Si layers decreased by 3 and 2.43 nm, respectively.

Analysis of the motion of a diffusion marker in an intermediate alloy, applied to a multilayer system [134], gives a simple expression for the ratio between Si and Sc partial diffusion coefficients:

$$R = \frac{D(\mathrm{Si})}{D(\mathrm{Sc})} = \frac{m}{n}\frac{\Delta X_1}{\Delta X_2}\,, \tag{32}$$

where ΔX_1 is the increase in distance X_1 between the Sc-on-ScSi interface and the diffusion marker, ΔX_2 is the increase in distance X_2 between the ScSi-on-Si interface and the diffusion marker (see the scheme in Fig. 13), and m/n is the ratio of the number of Sc atoms to the number of Si atoms in the silicide.

It is seen from Fig. 13 that $A = 2X_1 + h(\mathrm{Sc})$, and $B = 2X_2 + h(\mathrm{Si})$. Bearing in mind that interval A increases and interval B decreases during silicide growth, one finds

$$2\Delta X_1 = \Delta A + \Delta h(\mathrm{Sc})\,, \tag{33}$$

$$2\Delta X_2 = \Delta h(\mathrm{Si}) - \Delta B\,, \tag{34}$$

where ΔX_1, ΔA, $\Delta h(\mathrm{Sc})$, ΔX_2, $\Delta h(\mathrm{Si})$, and ΔB are changes in the absolute thicknesses of the respective layers and intervals. Since for ScSi silicide the coefficient $m/n = 1$, we finally arrive at

$$R = \frac{\Delta A + \Delta h(\mathrm{Sc})}{\Delta h(\mathrm{Si}) - \Delta B}\,. \tag{35}$$

The results of calculations of the ratio between partial diffusion coefficients, $R = D(\mathrm{Si})/D(\mathrm{Sc})$, are included in Table 2. The partial diffusion coefficient of silicon is higher than that of scandium. Thus, the growth of amorphous scandium silicide, ScSi, is limited by diffusion of Si atoms through the silicide layer to ScSi-on-Sc and Sc-on-ScSi interfaces, the main sites of silicide formation.

The large difference between partial diffusion coefficients is characteristic of many binary transition metal/silicon systems, especially those prone to solid-phase amorphization. In the latter case, diffusion asymmetry is considered to be a possible cause of, and even an indispensable condition for, kinetic stability of the amorphous phase with respect to the crystalline one [35]. Indeed, the growth of the amorphous silicide can occur via mass transfer of most mobile atoms alone, whereas reconstruction of the amorphous structure to the crystal lattice is only possible if both components of the binary system are mobile. This explains why, in certain cases, amorphization takes place, while crystallization does not, even if the two processes are governed by diffusion.

9. Diffusion and phase formation in molybdenum/silicon multilayer systems

9.1 Kinetics of phase formation in Mo/Si multilayer systems

The period of the primary multilayer structure was $H = 11.32$ nm. TEM studies [135, 136] showed that AIZ thickness at Mo-on-Si and Si-on-Mo interfaces was $h(\mathrm{Mo\text{-}on\text{-}Si}) = 1.2$ nm and $h(\mathrm{Si\text{-}on\text{-}Mo}) = 0.6$ nm, respectively. Annealing at 340 °C for 30 h increased the thickness of AIZs at both interfaces (by about 1 nm at Mo-on-Si, and by about 0.5 nm at the opposite Si-on-Mo interface). The AIZ growth rate at Mo-on-Si interface essentially exceeds the analogous parameter at opposite Si-on-Mo interface. The tendency to asymmetric growth of AIZs during fabrication of Mo/Si PMCs by isothermal annealing was observed to retain as described in Sections 4 and 7. The results of direct TEM studies were confirmed by simulation of small-angle X-ray diffraction spectra of initial and annealed PMCs by a four-layer model on the assumption of AIZ formation at both interfaces, with the average composition corresponding to molybdenum disilicide. The composition of the disilicide thus formed was described in our previous studies [100, 101, 103, 104].

The thickness of the AIZ after each annealing was determined by simulation of small-angle X-ray spectra. Certain values obtained by this method were verified by direct cross-sectional TEM, as in the case of Sc/Si multilayer systems. The fast growth of AIZ thickness at the early annealing stages markedly decelerated as annealing time increased, especially at the Si-on-Mo interface. Figure 14 displays kinetic curves (thickness squared of the $MoSi_2$ layer vs annealing time) of $MoSi_2$ disilicide growth at Mo-on-Si and Si-on-Mo interfaces, respectively, in an Mo/Si PMC annealed at 380 °C. The curves (see Fig. 14) were approximated based on the relaxation model [86–89] and formula (31), where h_0 is the AIZ thickness in initial multilayer structures equaling 1.2 and 0.6 nm at Mo-on-Si and Si-on-Mo interfaces, respectively.

The figure depicts that kinetic curves are fairly well described by the relaxation model for an amorphous substance. Equilibrium diffusion coefficients (D_{eq}) were estimated at 2.29×10^{-23} and 2.36×10^{-25} m^2 s^{-1} for Mo-on-Si and Si-on-Mo interfaces, respectively. This means that the diffusion coefficient during the parabolic growth of molybdenum disilicide at the Mo-on-Si interface is two orders of magnitude higher than that for Si-on-Mo. In what follows, we show that silicon is the dominant diffusing species in the Mo/Si system, and we discuss possible causes of the asymmetry of silicon diffusion coefficients at different interphase boundaries.

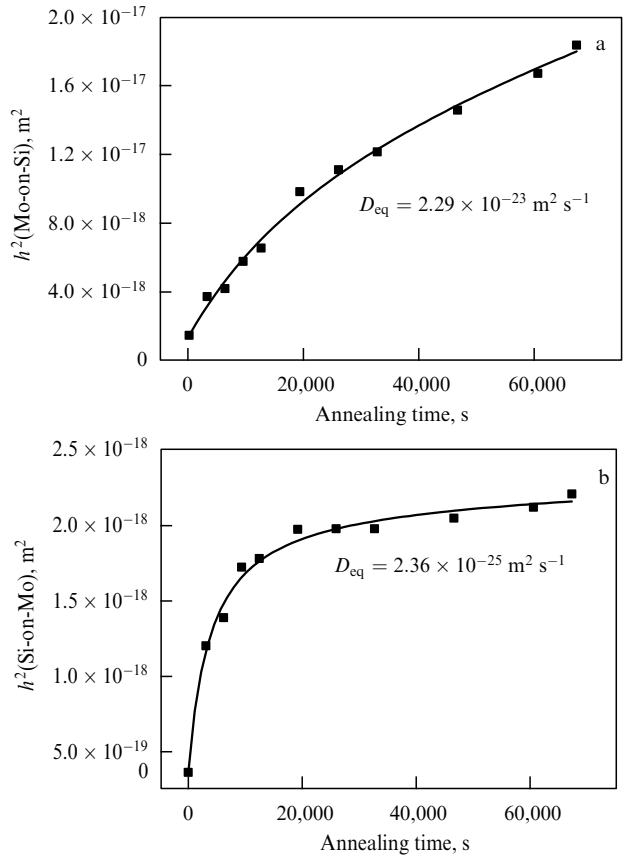

Figure 14. Thickness squared of molybdenum disilicide ($MoSi_2$) at Mo-on-Si (a) and Si-on-Mo (b) interfaces in an Mo/Si PMC at the annealing temperature of 380 °C plotted vs annealing time.

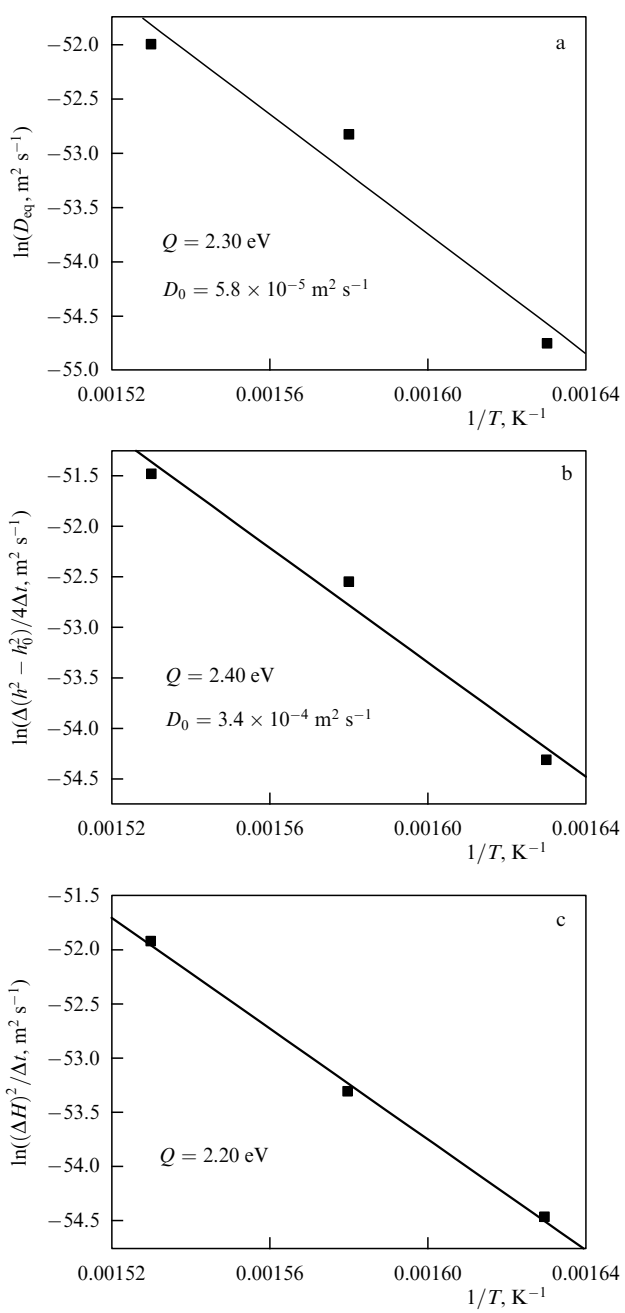

Figure 15. Arrhenius plots for equilibrium diffusion coefficients D_{eq} calculated from the relaxation model (a), from the slopes of annealing time dependences of $(h^2 - h_0^2)$ (b), and the slopes of annealing time dependences of ΔH^2 (c) at prolonged annealing.

Figure 15 presents Arrhenius plots for equilibrium diffusion coefficients D_{eq} calculated from the relaxation model (a), and from the slopes of annealing time dependences of $(h^2 - h_0^2)$ (b) and the slopes of annealing time dependences of ΔH^2 (c) at large annealing times. Activation energies derived from all three dependences are roughly similar (within the scatter of the measurement). According to formula (31), the equilibrium diffusion coefficient determines the diffusion coefficient at later annealing stages, when the parabolic law for diffusion is fulfilled, i.e., in the region of the linear dependence of $(h^2 - h_0^2)$ on the diffusion annealing time. The plot in Fig. 15b is constructed from the slopes of the linear approximation of the annealing time dependence of $(h^2 - h_0^2)$ in the linear section of this dependence. Given that the diffusion parabolic law is fulfilled, the $(h^2 - h_0^2)/t$ ratio is proportional to the diffusion coefficient. The plot in Fig. 15c is constructed from the slopes of the linear section of the annealing time dependence of ΔH^2, i.e., at large annealing times. The thickness of the silicide formed during annealing is proportional to the decrease in the PMC period [see formula (21)]. It follows from Fig. 14b that the growth rate of the AIZ at the Si-on-Mo interface slows down substantially at large annealing times. In other words, a change in the PMC period is determined in this case largely by the increase in the AIZ thickness at the Mo-on-Si interface. For this reason, all three above-depicted Arrhenius plots reflect a change of the diffusion coefficient in the region of silicide parabolic growth at the Mo-on-Si interface. Therefore, activation energies derived from the three dependences are rather similar ($Q = 2.2-2.4$ eV). A close value ($Q = 2.4$ eV) was reported in paper [80], where the thickness of amorphous silicide interlayers in annealed Mo/Si PMCs with the period $H \approx 7$ nm was measured by direct cross-sectional TEM.

9.2 Structure, diffusion, and phase formation in Mo/Si multilayer compositions fabricated with the substrate bias potential

The structural state of primary Mo/Si multilayer compositions with the period $H \approx 35$ nm, fabricated with the use of substrate bias potentials $U_b(\text{Si}) = -75$ V and $U_b(\text{Mo}) = -50$ V for silicon and molybdenum layers, respectively, is characterized by a high level of mechanical stress in the molybdenum layer. The tilt-scanning technique ($\sin^2\psi$ method) was utilized to determine stresses and Mo lattice period in stress-

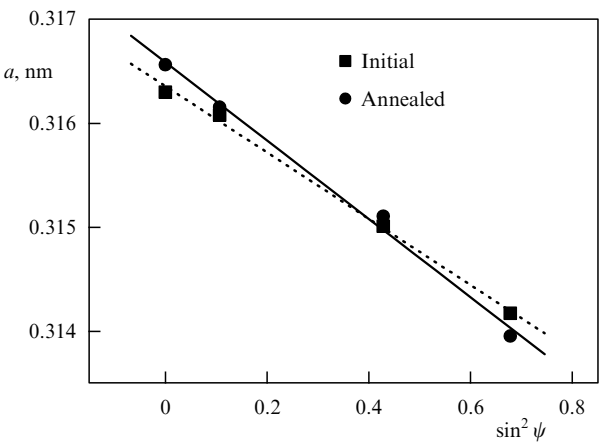

Figure 16. The plot of molybdenum lattice parameter vs $\sin^2\psi$ of initial and annealed ($T_{an} = 400\,^\circ$C, for 5 h) samples. ψ is the angle between the reflecting planes and the plane of the location of the multilayer composition layers.

free cross sections (a_0) through primary and annealed samples. The lattice periods a necessary to construct ($a - \sin^2\psi$) plots were calculated from the angular position of diffraction maxima from {321} and {220} type planes with different tilt angles ψ with respect to the surface. Strains ε_{11} and stresses σ_{11} were determined using a model of symmetrical biaxial stressed state [137] by the formulas

$$\varepsilon_{11} = \frac{a_{11} - a_0}{a_0}\,, \tag{36}$$

$$\sigma_{11} = \frac{1}{1-\nu}\,\varepsilon_{11}E\,, \tag{37}$$

where a_{11} is the Mo lattice period in the plane of the multilayer composition, derived by extrapolation of plot ($a - \sin^2\psi$) to the value of $\sin^2\psi = 1$; a_0 is the Mo lattice period in the stress-free cross section, derived from plot ($a - \sin^2\psi$) at $\sin^2\psi_0 = 2\nu/(1+\nu) = 0.466$; $\nu = 0.304$ is the Poisson coefficient [138], and $E = 3.178 \times 10^5$ MPa is Young's modulus [138].

Figure 16 displays plots for initial and annealed ($T_{an} = 400\,^\circ$C, for 5 h) samples. The former undergoes strong compressive strains and stresses ($\varepsilon_{11} = -5.4 \times 10^{-3}$ and $\sigma_{11} = -2467$ MPa). The experimentally found period of Mo lattice, $a_0 = 0.31487$ nm, is close to the tabulated value of 0.31474 nm [138]. The lattice period in the stress-free state is practically independent of annealing time and remains $a_0 = 0.31483$ nm. The high level of compressive stresses in Mo layers is due to the use of the bias potential $U_b(\text{Mo}) = -50$ V during their deposition. The application of the bias potential leads to the extraction of Ar^+ ions from the magnetron discharge plasma, ion bombardment of the growing Mo surface, and the generation of self-interstitial atoms. These atoms are deposited on edge dislocations or make up interstitial loops, giving rise to additional nodes in the Mo film and generating compressive stress [139, 140]. Compressive strains and stresses in the Mo layer increase during annealing, compared with initial values, to $\varepsilon_{11} = -6.4 \times 10^{-3}$ and $\sigma_{11} = -2918$ MPa, respectively.

Figure 17 presents TEM images of the samples annealed at 350 °C for 40 h, and at 400 °C for 3 h. The initial sample image is displayed in Fig. 5c. Evidently, the silicide phase grows only from the Mo-on-Si interface and the three-layer structure of the PMC remains unaltered. Both TEM images of the annealed samples display crystals in the silicide layers, testifying to their crystalline structure under the given annealing conditions. Moreover, there is an additional layer (lighter than silicon) at the $MoSi_2$-on-Si interface visible at lower magnifications and strong underfocusing ($\sim$ 200 nm) of the objective lens (Fig. 18). This layer is well apparent at large annealing times and a large enough thickness of the silicide layer. Usually, such phase contrast is characteristic of precipitates with lower density compared with the matrix [141]; it has also been observed in small pores [142]. Certain cross-sectional TEM images display lamination of PMC along these lower-density layers. The total silicide thickness under the given annealing conditions was roughly equal ($\sim$ 6.5 nm). The initial thickness being 1.4 nm, this means that annealing gave rise to an additional silicide layer with thickness $\Delta h(MoSi_2) \sim 5.1$ nm.

The annealed samples have substantially modified small-angle X-ray diffraction spectra compared with those of the primary specimen. These spectra contain only 17 Bragg peaks, against 25 in the initial PMC. Extinction of long-range order reflections is attributable to increased interface roughness and related to the growth of crystalline Mo disilicide, as appears from the cross-sectional micrographs of annealed samples in Fig. 17.

Molybdenum disilicide formed even at the highest annealing temperature (400 °C) exhibits poor crystalline perfection and is difficult to detect by diffraction techniques. Large-angle X-ray diffractometry of annealed samples reveals only peaks of crystalline molybdenum. The strongest

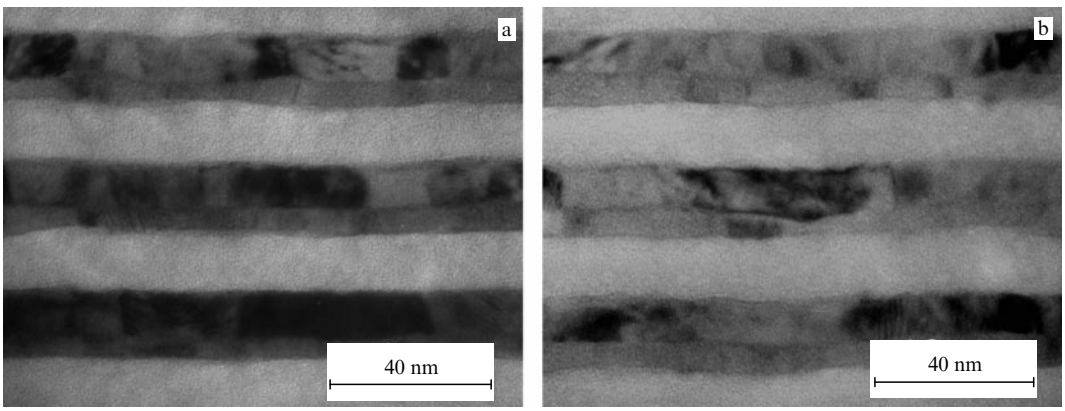

Figure 17. TEM images of a sample annealed at $T_{an} = 350\,^\circ$C for 40 h, $H = 32.8$ nm (a), and at $T_{an} = 400\,^\circ$C for 3 h, $H = 33$ nm (b). The underlying silicon substrate is not shown.

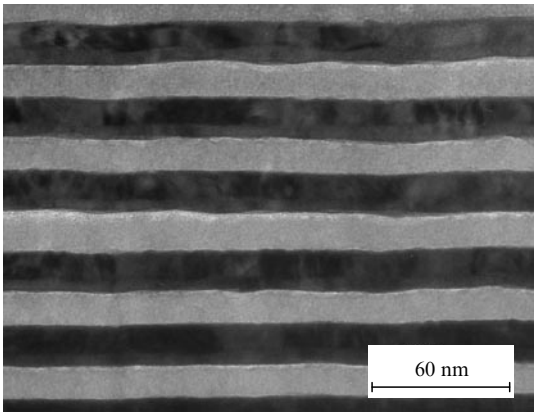

Figure 18. TEM image of a sample annealed at 350 °C for 40 h [strong underfocusing (∼ 200 nm) of the objective lens]. The underlying silicon substrate is not shown.

(110) diffraction peak is shifted approximately by 0.3° toward smaller angles from those of the tabulated value, which suggests large compressive stress in Mo layers. The intensity of the (110) diffraction peak decreases at large annealing times, while its angular position remains virtually unaltered. Indeed, precision measurements of the lattice period indicate that strains in the Mo layer change but insignificantly during isothermal annealing.

TEM images of primary and annealed samples were used to estimate consumption of the starting components (Mo and Si) and elucidate the composition of the silicide phase formed in the course of annealing. This silicide corresponds to Mo disilicide, $MoSi_2$, with density $\rho = 5.6$ g cm^{-3} that is roughly 10% lower than the tabulated value ($\rho = 6.26$ g cm^{-3}). This is quite natural for such low annealing temperatures responsible for the imperfection of the disilicide structure.

Figure 19a gives changes in PMC period with annealing time at 350 °C. This dependence can be arbitrarily divided into three sections:

I. $0 \leqslant \Delta H \leqslant 0.5-0.6$ nm — strong period reduction section;

II. $0.5-0.6 \leqslant \Delta H \leqslant 1.1$ nm — moderate period reduction section,

III. $\Delta H \geqslant 1.1$ nm — weak period reduction section.

The dependence of the thickness of the resulting $MoSi_2$ disilicide on the annealing time, calculated from formula (21) for densities $\rho(MoSi_2) = 6.26$ and 5.6 g cm^{-3}, is illustrated in Fig. 19b. Evidently, the thicknesses measured directly from TEM images fairly well coincide with theoretical ones for density $\rho(MoSi_2) = 5.6$ g cm^{-3}. Figure 19c shows the annealing time dependence of $(h^2 - h_0^2)$ for the Mo disilicide density of 5.6 g cm^{-3}. The values of h are appropriate to the total thickness of silicide formed during sample preparation and subsequent annealing. The value of $h_0 = 1.4$ nm corresponds to the thickness of the disilicide formed during sample preparation to the experiment.

The lower-density layer at the $MoSi_2$-on-Si interface forms as a result of Si departure from the pure silicon layer. At this site, the excess free volume transforms into micropores. Silicon atoms are transported from the pure silicon layer across the growing Mo disilicide toward the Mo-on-$MoSi_2$ interface where the chemical reaction runs and gives rise to this disilicide.

In the PMCs under consideration with a high level of compressive stress in the molybdenum layers, Mo disilicide

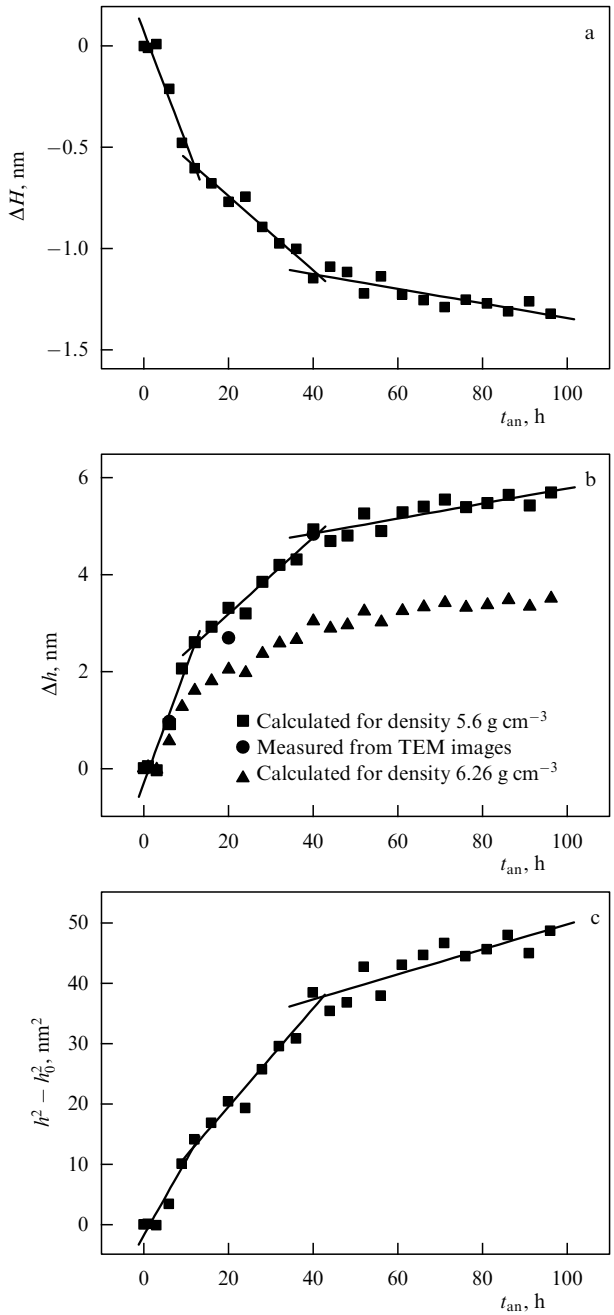

Figure 19. PMC period variations (ΔH) plotted vs annealing time (a); variations of $MoSi_2$ disilicide thickness (Δh) calculated by formula (21) for $MoSi_2$ disilicide densities $\rho(MoSi_2) = 6.26$ and 5.6 g cm^{-3}, and silicide layer thickness measured from TEM images (b); variations of the difference between the squares of total Mo (h^2) and initial Mo (h_0^2) disilicide thicknesses depending on isothermal annealing time at 350 °C (c).

forms only from the Mo-on-Si interface due to the nonuniform distribution of compressive stress. As shown before, stresses in molybdenum layers increase during annealing from −2.5 to −2.9 GPa. Around 2 nm of molybdenum is consumed for silicide formation. The nonuniform distribution of stresses in the molybdenum layer is largely due to their higher level at the Si-on-Mo interface and can be accounted for by peculiar growth patterns of the magnetron-sputtered molybdenum layer. Bombardment of the growing molybdenum surface by Ar^+ ions creates compressive stress. On the other hand, the crystalline structure of the molybdenum layer improves as its thickness increases. Specifically, amorphous

molybdenum undergoes crystallization and subsequent recrystallization. These processes are accompanied by a decrease in the specific volume of Mo in the growing layer, which creates tensile stress. In other words, molybdenum layers far from the Mo-on-Si interface undergo strong compressive stress that relaxes or even merges into tensile stress near this interface due to improvement in the crystalline structure of these layers at the early stages of their growth. Stress variations in growing molybdenum layers were observed in Ref. [143] in single-layer Mo films and multilayer Mo/Si compositions fabricated by magnetron sputtering. Compressive stress reduces vacancy concentration in the Mo layer. While compressive stress increases toward the growing surface, the gradient of vacancy concentrations, on the contrary, is directed deep into the growing film. The similarity of Mo and Si atomic radii accounts for the generation of a substitution solid solution in Mo/Si systems and the substitutional mechanism of Si atom diffusion in crystalline Mo. The low vacancy concentration in the molybdenum layer near the Si-on-Mo interface hampers penetration of Si atoms into this layer and silicide phase formation at this interface. Strong compressive stress in the molybdenum layer close to the Si-on-Mo interface also interferes with the formation of AIZs in the primary samples.

If diffusion is the limiting process, the quantity $\Delta(h^2 - h_0^2)/\Delta t$ is proportional to the diffusion coefficient. Figure 20 shows the Arrhenius dependences for diffusion-governed kinetics. The activation energy is 2.20 ± 0.15 eV, 2.13 ± 0.21 eV, and 2.34 ± 0.22 eV for sections I, II, and III, respectively. The pre-exponential factor for the section III is $D_0 = 1.04 \times 10^{-4}\ \mathrm{m^2\,s^{-1}}$. In other words, the values of activation energy, diffusion coefficients, and pre-exponential factors measured for stressed molybdenum layers are similar to those for multilayer structures with stress-free molybdenum layers (see Section 9.1).

Our TEM studies showed that crystals appear in the silicide layer after annealing at 350 °C for 20 h, and at 400 °C for 1 h. These points correspond to the beginning of section II ($0.5-0.6 \leqslant \Delta H \leqslant 1.1$ nm) of period alteration (Fig. 19a, b). Thus, Mo disilicide has a crystalline structure in sections II and III of period changes over the entire range of annealing temperatures, $350 \leqslant T_{\mathrm{an}} \leqslant 400$ °C. An amorphous intermediate phase grows at the interfaces at early annealing stages ($0 \leqslant \Delta H \leqslant 0.5-0.6$ nm). TEM images of the samples annealed at 350 °C for 6 h, and at 400 °C for 0.5 h show the silicide layer containing no crystalline grains.

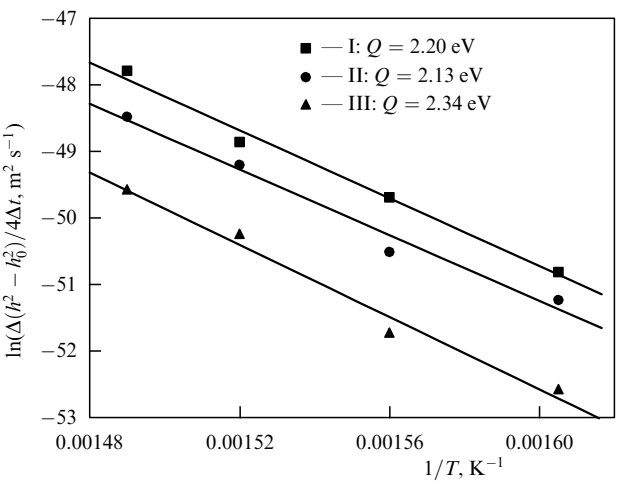

Figure 20. Arrhenius plots for kinetics governed by silicon atom diffusion through an Mo disilicide layer: I — strong period reduction section, II — moderate period reduction section, and III — weak period reduction section.

Despite the different structural states of the silicide phase at the early and late annealing stages, the found activation energies are identical (within the scatter of the measurement). They do not differ for amorphous and crystalline Mo disilicides due to the imperfection of the latter's structure.

In this case, the kinetic curves (dependence of h^2 on annealing time) cannot be described in terms of a relaxation model for an amorphous substance [86, 89] as in the case of Sc/Si and Mo/Si multilayer structures in the absence of compressive stress in molybdenum layers. At small temperatures (< 370 °C) and annealing times, the strong period reduction section I is preceded by a section of slower period reduction, i.e., a slower growth rate of the silicide phase. The slowed growth of this phase at initial annealing stages is not observed in Sc/Si and Mo/Si PMCs obtained without the use of the bias potential during the deposition of the metal layer. The author is unaware of any report on this effect in the voluminous literature on the annealing of metal/silicon multilayer structures. Usually, the maximum change of the period occurs at the earliest stages of annealing of such systems, as was observed in the present work and numerous experiments by other authors with Sc/Si and Mo/Si multilayer structures.

The slowdown effect in silicide phase growth at initial annealing stages may be related to other processes, e.g. the passage of diffusing Si atoms across the $MoSi_2$-on-Si interface. The use of the bias potential for deposition of multilayer coatings leads to a rise in Ar atom concentration [4]. Large argon atoms accumulated at the $MoSi_2$-on-Si interface will create strong local compressive stress, hampering penetration of Si atoms through the interface. For some time, this process is limiting. As Si atoms depart, the remaining voids interact with Ar atoms and give rise to the nuclei of argon-filled micropores. As a result, local strains weakens. This inference is confirmed by the presence of micropores at the $MoSi_2$-on-Si interface, visible in TEM images (see Fig. 18). It should be noted that micropores are absent at the interfaces of annealed Sc/Si and Mo/Si PMCs obtained without the use of bias potentials.

10. Conclusion. Peculiarities of diffusion and phase formation in periodic Sc/Si and Mo/Si multilayer coatings

The first phase to be formed at interfaces of Sc/Si multilayer coatings during their synthesis and annealing is an amorphous alloy with a chemical composition close to ScSi silicide. Silicon atoms are the dominant diffusant in the Sc/Si binary system. They travel from the pure silicon layer through the ScSi silicide layer toward Sc-on-ScSi and ScSi-on-Sc interfaces, where the reaction of silicide formation occurs. Diffusion of Si atoms is characterized by the small activation energy ($Q = 1$ eV) and pre-exponential factor ($D_0 = 4 \times 10^{-12}\ \mathrm{m^2\,s^{-1}}$). Such low diffusion parameters are typical of the diffusion of atoms with small radii in metallic glasses, e.g. diffusion of ^{57}Co isotope in the amorphous $Co_{89}Zr_{11}$ alloy. Also, such low activation energies and pre-exponential factors are intrinsic in small atoms diffusing in transition metals via an interstitial mechanism. In contrast, the diffusion parameters of large atoms, e.g. ^{195}Au isotope, in

the same amorphous $Co_{89}Zr_{11}$ alloy are indicative of the involvement of the substitutional mechanism of diffusion. Scandium and silicon atoms have essentially different radii (0.162 and 0.132 nm, respectively). An amorphous solid consisting of atoms with different radii must have two types of voids: long-lived small ones analogous to interstices in metals, and short-lived large ones analogous to vacancies. Vacancies are unstable in amorphous solids due to the lack of translational symmetry and viscous flow in them.Therefore, large voids can arise in amorphous matter only via fluctuations, due to the local redistribution of the free volume, and have a short lifetime. Small values of activation energy and the pre-exponential factor suggest that silicon atoms in ScSi disilicide diffuse through small long-lived voids.

Owing to the low activation energy, diffusion of silicon atoms in the amorphous ScSi alloy begins at a low annealing temperature ($\sim 100\,^{\circ}$C). At the initial stages, silicide growth does not obey the parabolic diffusion law ($h^2 \sim t$) and proceeds at an accelerated rate. After a certain critical thickness (isothermal annealing time) is reached, kinetic curves are fairly well described by the parabolic law. The critical thickness depends on annealing temperature, and increases as it rises. The entire kinetic curve is well described by the relaxation model of an amorphous solid. The excess free volume is contracted during annealing; simultaneously, the diffusion coefficient decreases. The annealing temperature dependence of critical thickness indicates that silicon atoms diffuse through the growing silicide layer faster than it relaxes under the influence of viscous flow. For diffusion to occur and an amorphous silicide to be formed, only one component (in the present case, silicon) may be mobile. In contrast, viscous flow is due to the mobility of both components.

The structural state and stresses of metal layers are known to influence phase formation kinetics in periodic Mo/Si multilayer coatings. In such compositions fabricated with the use of the bias potential and characterized by a high level of compressive stress (around -2.5 GPa), Mo disilicide grows in molybdenum layers only from the Mo-on-Si interface. No silicide growth at the opposite Si-on-Mo interface is observed by cross-sectional TEM, even at very large annealing times. Silicon atoms make up the dominant diffusant in PMCs. Si atoms diffuse from the pure silicon layer through the Mo disilicide layer and reach the Mo-on-$MoSi_2$ interface, where the solid-phase reaction yields silicide. Clearly, the silicide grows in a similar manner at the opposite $MoSi_2$-on-Mo interface, but the growth rate here is rather low. Moreover, in a certain structural state of the molybdenum layer, no silicide forms at this interface. Therefore, diffusion characteristics for the Mo-on-Si interface were obtained in the present work. The activation energy and pre-exponential factor in the expression for the diffusion coefficient of Si atoms through the Mo disilicide layer during parabolic growth were $Q = 2.3$ eV and $D_0 = 6 \times 10^{-5}$ m^2 s^{-1} for PMCs obtained without the bias potential, and $Q = 2.34$ eV and $D_0 = 1 \times 10^{-4}$ m^2 s^{-1} for PMCs fabricated with the use of the bias potential. Evidently, the respective values are very similar. They are typical of atomic diffusion in substitution crystalline alloys by the vacancy mechanism. These parameters do not change (within the scatter of the measurement) when the amorphous molybdenum disilicide turns into the crystalline one. The high-temperature metastable hexagonal Mo disilicide having poor structural perfection is the first to crystallize at low annealing temperatures. Molybdenum and silicon have similar atomic radii [r(Mo) $= 0.139$ nm, and r(Si) $= 0.132$ nm] and form a substitution solid silicon solution in molybdenum. This binary Mo/Si system differs from the binary Sc/Si structure in which the two components have significantly different atomic radii. The difference between silicon and metal radii is responsible for the considerable difference between diffusion characteristics (activation energy and pre-exponential factor) of silicon in silicide, and between processes of solid-phase amorphization and crystallization of amorphous silicide. As noted, the values of the above diffusion characteristics of silicon in molybdenum disilicide are typical of the substitutional mechanism of diffusion. This means that silicon diffusion in amorphous silicide occurs through sufficiently large vacancy-like cavities.

Acknowledgments. The author gratefully acknowledges his colleagues and co-authors V V Kondratenko, V A Sevryukova, Yu P Pershin, D L Voronov, A V Pen'kov, V I Pinegin, A V Vinogradov, Yu A Uspensky, I A Artyukov, and S A Yulin for assistance in this work, useful discussions of the results, and preparation of the present article.

References

1. Geguzin Ya E *Diffuzionnaya Zona* (Diffusion Zone) (Moscow: Nauka, 1979)
2. Tu K-N, Mayer J W, Feldman L C *Electronic Thin Film Science: for Electrical Engineers and Materials Scientists* (New York: Macmillan, 1992)
3. Brik V B *Diffuziya i Fazovye Prevrashcheniya v Metallakh i Splavakh* (Diffusion and Phase Transformations in Metals and Alloys) (Kiev: Naukova Dumka, 1985)
4. Holloway K, Do K B, Sinclair R *J. Appl. Phys.* **65** 474 (1989)
5. Murarka S P *Silicides for VLSK Applications* (New York: Academic Press, 1983) [Translated into Russian (Moscow: Mir, 1986)]
6. Poate J M, Tu K N, Mayer J W (Eds) *Thin Films: Interdiffusion and Reactions* (New York: Wiley, 1978) [Translated into Russian (Moscow: Mir, 1982)]
7. Walser R M, Bene R W *Appl. Phys. Lett.* **28** 624 (1976)
8. Shewmon P G *Diffusion in Solids* (New York: McGraw-Hill, 1963) [Translated into Russian (Moscow: Metallurgiya, 1966)]
9. Mader S *Thin Solid Films* **35** 195 (1976)
10. Gösele U, Tu K N *J. Appl. Phys.* **53** 3252 (1982)
11. Tu K N *Annu. Rev. Mater. Sci.* **15** 147 (1985)
12. Schwarz R B, Johnson W L *Phys. Rev. Lett.* **51** 415 (1983)
13. Koch C C et al. *Appl. Phys. Lett.* **43** 1017 (1983)
14. Cotts E J, Meng W J, Johnson W L *Phys. Rev. Lett.* **57** 2295 (1986)
15. Cotts E J, Wong G C, Johnson W L *Phys. Rev. B* **37** 9049 (1988)
16. Meng W J, Nieh C W, Johnson W L *Appl. Phys. Lett.* **51** 1693 (1987)
17. Dörner W, Mehrer H *Phys. Rev. B* **44** 101 (1991)
18. Donovan E P et al. *J. Appl. Phys.* **57** 1795 (1985)
19. Donovan E P et al. *Appl. Phys. Lett.* **42** 698 (1983)
20. Petford-Long A K et al. *J. Appl. Phys.* **61** 1422 (1987)
21. Bugaev E A et al. *Surface Investigation* **15** 141 (1999)
22. Slaughter J M et al. *Pros. SPIE* **1343** 73 (1991)
23. Holloway K, Sinclair R *J. Appl. Phys.* **61** 1359 (1987)
24. Holloway K, Sinclair R *J. Less Common Met.* **140** 139 (1988)
25. Nathan M *J. Appl. Phys.* **63** 5534 (1988)
26. Gong S F et al. *J. Appl. Phys.* **68** 4535 (1990)
27. Ma E et al. *Appl. Phys. Lett.* **53** 2033 (1988)
28. Wang W H, Wang W K *J. Appl. Phys.* **76** 1578 (1994)
29. Tu K N, Herd S R, Gösele U *Phys. Rev. B* **43** 1198 (1991)
30. Chen J C, Shen G H, Chen L J *J. Appl. Phys.* **84** 6083 (1998)
31. Kjornrattanawanich B et al. *Appl. Opt.* **45** 1765 (2006)
32. Gong S F, Hentzell H T G *J. Appl. Phys.* **68** 4542 (1990)
33. Miedema A R *J. Less Common Met.* **46** 67 (1976)
34. Bene R W *J. Appl. Phys.* **61** 1826 (1987)
35. Gösele U, Tu K N *J. Appl. Phys.* **66** 2619 (1989)
36. Stearns D G, Rosen R S, Vernon S P *Proc. SPIE* **1547** 2 (1992)
37. Slaughter J M et al. *J. Appl. Phys.* **76** 2144 (1994)
38. Andreev S S et al. *Thin Solid Films* **415** 123 (2002)
39. Becker H et al. *Proc. SPIE* **4688** 503 (2002)
40. Bajt S, Stearns D G, Kearney P A *J. Appl. Phys.* **90** 1017 (2001)
41. Stearns M B, Chang C-H, Stearns D G *J. Appl. Phys.* **71** 187 (1992)

42. Voorma H-J et al. *J. Appl. Phys.* **83** 4700 (1998)
43. Niibe M et al. *Proc. SPIE* **1343** 2 (1991)
44. Voorma H-J et al. *J. Appl. Phys.* **82** 1876 (1997)
45. Yakshin A E et al. *Physica B* **283** 143 (2000)
46. Cilia M, Verhoeven J *J. Appl. Phys.* **82** 4137 (1997)
47. Cheng Y et al. *J. Appl. Phys.* **72** 5165 (1992)
48. Stearns D G et al. *J. Appl. Phys.* **67** 2415 (1990)
49. Windt D L, Hull R, Waskiewicz W K *J. Appl. Phys.* **71** 2675 (1992)
50. Boercker D B, Morgan W L *Proc. SPIE* **1547** 47 (1992)
51. Slaughter J M et al. *Phys. Rev. B* **44** 3854 (1991)
52. Bedrossian P J *Surf. Sci.* **320** 247 (1994)
53. Bedrossian P J *Surf. Sci.* **322** 73 (1995)
54. Vernon S P, Stearns D G, Rosen R S *Appl. Opt.* **32** 6969 (1993)
55. Hasan M M, Highmore R J, Somekh R E *Vacuum* **43** 55 (1992)
56. Birch J et al. *Vacuum* **68** 275 (2002)
57. Zhou X W, Wadley H N G *J. Appl. Phys.* **84** 2301 (1998)
58. Eriksson F et al. *Thin Solid Films* **500** 84 (2006)
59. Louis E et al. *Proc. SPIE* **3997** 406 (2000)
60. Folta J A et al. *Proc. SPIE* **3676** 702 (1999)
61. Bajt S et al. *Proc. SPIE* **4506** 65 (2000)
62. Shimizu M et al. *Jpn. J. Appl. Phys.* **32** 4074 (1993)
63. Feigl T et al. *Proc. SPIE* **3997** 420 (2000)
64. Yulin S A et al. *Proc. SPIE* **4343** 607 (2001)
65. Yulin S A et al. *Proc. SPIE* **5645** 289 (2005)
66. Yulin S et al. *Proc. SPIE* **5751** 1155 (2005)
67. Yulin S et al. *Microelectron. Eng.* **83** 692 (2006)
68. Gautier J et al. *Appl. Opt.* **44** 384 (2005)
69. Shih W C, Stobbs W M *Ultramicroscopy* **32** 219 (1990)
70. Burkhalter P G et al. *J. Vac. Sci. Technol. B* **9** 845 (1991)
71. Kortright J B, Joksch St, Ziegler E *J. Appl. Phys.* **69** 168 (1991)
72. Windt D L *J. Vac. Sci. Technol. A* **18** 980 (2000)
73. Salditt T, Metzger T H, Peisl J *Phys. Rev. Lett.* **73** 2228 (1994)
74. Salditt T et al. *Phys. Rev. B* **54** 5860 (1996)
75. Windt D L et al. *J. Appl. Phys.* **88** 460 (2000)
76. Bower R W, Mayer J W *Appl. Phys. Lett.* **20** 359 (1972)
77. Guivarc'h A et al. *J. Appl. Phys.* **49** 233 (1978)
78. Bravman J C, Sinclair R *J. Electron. Microsc. Tech.* **1** 53 (1984)
79. Cheng J Y, Cheng H G, Chen L J *J. Appl. Phys.* **61** 2218 (1987)
80. Rosen R S et al. *Appl. Opt.* **32** 6975 (1993)
81. Cage P R, Bartlett R W *Trans. Metall. Soc. AIME* **233** 832 (1965)
82. Sloof W G et al. *Scripta Metall.* **20** 1683 (1986)
83. Nakajima H, Fujimori H, Masahiro K *J. Appl. Phys.* **63** 1046 (1988)
84. Wang W-H et al. *Phys. Rev. B* **59** 10811 (1999)
85. Cook H E, Hilliard J E *J. Appl. Phys.* **40** 2191 (1969)
86. Loopstra O B et al. *Phys. Rev. B* **44** 13519 (1991)
87. Cohen M H, Turnbull D *J. Chem. Phys.* **31** 1164 (1959)
88. Cohen M H, Grest G S *Phys. Rev. B* **20** 1077 (1979)
89. Spaepen F *Mater. Sci. Eng.* **97** 403 (1988)
90. Sietsma J, Thijsse B J *Phys. Rev. B* **52** 3248 (1995)
91. Danilin B S, Syrchin V K *Magnetronnye Raspylitel'nye Sistemy* (Magnetron Sputtering Systems) (Moscow: Radio i Svyaz', 1982)
92. Patelli A et al. *Surf. Coat. Technol.* **201** 143 (2006)
93. Somekh R E *J. Vac. Sci. Technol. A* **2** 1285 (1984)
94. Williams D B, Carter B C *Transmission Electron Microscopy: A Textbook for Materials Science* (New York: Springer Science Business Media, 2009)
95. Barbee T W *Opt. Eng.* **25** 899 (1986)
96. Spiller E *Soft X-Ray Optics* (Washington: SPIE Optical Engineering Press, 1994)
97. Stearns D G *J. Appl. Phys.* **65** 491 (1989)
98. Vinogradov A V et al. *Zerkal'naya Rentgenovskaya Optika* (Mirror X-ray Optics) (Ed. A V Vinogradov) (Leningrad: Mashinostroenie, 1989)
99. Zubarev E N et al. *Metallofiz. Noveishie Tekhnol.* (8) 56 (1997)
100. Yulin S et al. *J. Appl. Phys.* **92** 1216 (2002)
101. Zubarev E N et al. *Poverkhnost': Rentgen. Sinkhrotron. Neitron. Issled.* (2) 20 (2002)
102. Zubarev E N et al., in *Tezisy Dokladov IX Natsional'noi Konf. po Rostu Kristallov, 16 – 20 Oktyabrya 2000, Moskva* (IX National Conf. on Crystal Growth, 16 – 20 October 2000, Moscow. Abstracts) (Moscow: IK RAN, 2000) p. 528
103. Kondratenko V V et al. *Appl. Opt.* **32** 1811 (1993)
104. Fedorenko A I et al. *Funktsional'nye Mater.* (2) 33 (1994)
105. Zubarev E N et al. *Metallofiz. Noveishie Tekhnol.* (10) 429 (2002)
106. Pinegyn V I et al. *Thin Solid Films* **516** 2973 (2008)
107. Zubarev E N et al., in *Book Abstracts of 12th Intern. Conf. on Thin Films, Bratislava, Slovakia 15 – 20 September 2002*, p. 212
108. Nastasi M, Mayer J W *Mater. Sci. Eng. R* **12** 1 (1994)
109. Volobuev V V et al., in *Nauchnye Trudy NAN Ukrainy: Nanostrukturnye Materialy* (Research on Nanoscale Materials, Ukrainian Academy of Sciences) (Kiev: Inst. Problem Materialovedeniya, 1998) p. 141
110. Uspenskii Yu A et al. *Opt. Lett.* **23** 771 (1998)
111. Uspenskii Yu A et al. *Surface Investigation* **15** 103 (1999)
112. Uspenskii Yu A et al. *Nucl. Instrum. Meth. Phys. Res. A* **448** 147 (2000)
113. Fedorenko A I et al. *J. X-Ray Sci. Technol.* (9) 35 (2001)
114. Zubarev E N et al. *Vestn. Khar'kovskogo Nats. Univ. Fiz.* (739) 141 (2006)
115. Voronov D L et al., in *Tezisy Dokladov IX Natsional'noi Konf. po Rostu Kristallov, 16 – 20 Oktyabrya 2000, Moskva* (IX National Conf. on Crystal Growth, 16 – 20 October 2000, Moscow. Abstracts) (Moscow: IK RAN, 2000) p. 529
116. Voronov D L et al., in *Rentgenovskaya Optika — 2001: Materialy Soveshch., Nizhnii Novgorod, 19 – 22 Fevralya 2001* (X-ray Optics — 2001. Proc., Nizhnii Novgorod, 19 – 22 February 2001) (Nizhny Novgorod: Inst. Fiziki Mikrostruktur RAN, 2001) p. 48
117. Vinogradov A V et al. *Proc. SPIE* **4505** 230 (2001)
118. Voronov D L et al. *Poverkhnost'. Rentgen. Sinkhrotron. Neitron. Issled.* (1) 6 (2002)
119. Voronov D L et al. *AIP Conf. Proc.* **641** 575 (2002)
120. Voronov D L et al. *Poverkhnost'. Rentgen. Sinkhrotron. Neitron. Issled.* (5) 13 (2007)
121. Voronov D L et al., in *Book Abstracts of 10th Intern. Conf. on X-Ray Lasers, Berlin, Germany 21 – 25 August 2006*, p. 115
122. Voronov D L et al. *Functional Mater.* (5) 856 (1999)
123. Voronov D L et al. *Functional Mater.* **15** (1) 30 (2008)
124. Voronov D L et al., in *Materialy V Mezhdunar. Konf. 'Nelineinye Protsessy i Problemy Samoorganizatsii v Sovremennom Materialovedenii', 3 – 5 Oktyabrya 2004, Voronezh* (Proc. V Intern. Conf. 'Nonlinear Processes and Problems of Self-Organization in Modern Materials Science', 3 – 5 October 2004, Voronezh) Vol. 1 (Voronezh, 2004) p. 117
125. Voronov D L et al., in *Book Abstracts of the 9th Intern. Conf. on the Physics of X-ray Multilayer Structures, Montana, USA 3 – 7 February 2008*, p. 2.3
126. Voronov D L et al. *Poverkhnost'. Rentgen. Sinkhrotron. Neitron. Issled.* (2) 75 (2002)
127. Voronov D L et al. *Functional Mater.* **9** (3) 534 (2002)
128. Voronov D L et al., in *Rentgenovskaya Optika-99. Materialy Soveshch., Nizhnii Novgorod, 1 – 4 Marta 1999* (X-ray Optics — 1999. Proc., Nizhnii Novgorod, 1 – 4 March 1999) (Nizhny Novgorod: Inst. Fiziki Mikrostruktur RAN, 1999) p. 138
129. Voronov D L et al., in *Materialy Tret'ego Mezhdunar. Nauchn. Seminara 'Sovremennye Metody Analiza Diffraktsionnykh Dannykh (Topografiya, Diffraktometriya, Elektronnaya Mikroskopiya)', 22 – 25 Maya 2006, Veliky Novgorod* (Proc. 3rd Intern. Workshop on Modern Methods of Analysis of Diffraction Data (Topography, Diffractometry, Electron Microscopy), 22 – 25 May 2006, Veliky Novgorod) (Veliky Novgorod, 2006) p. 135
130. Kotroczo V, McColm I J *J. Alloys Compounds* **203** 259 (1994)
131. Samsonov G V, Dvorina L A, Rud' B M *Silitsidy* (Silicides) (Moscow: Metallurgiya, 1979)
132. Tardy J, Tu K N *Phys. Rev. B* **32** 2070 (1985)
133. Voronov D L et al. *Thin Solid Films* **513** 152 (2006)
134. Gösele U, Tu K N, Thompson R D *J. Appl. Phys.* **53** 8759 (1982)
135. Penkov A V et al. *Functional Mater.* **12** (4) 750 (2005)
136. Devizenko O Yu et al., in *Abstract Book of the Intern. Conf. Crystal Materials' 2005* (Kharkov, 2005) p. 211
137. Palatnik L S, Fuks M Ya, Kosevich V M *Mekhanizm Obrazovaniya i Substruktura Kondensirovannykh Plenok* (Mechanism of Formation and Substructure of Condensed Films) (Moscow: Nauka, 1972)
138. Frantsevich I P, Voronov F F, Bakuta S A *Uprugie Postoyannye i Moduli Uprugosti Metallov i Nemetallov*. Spravochnik (Elastic Constants and Coefficients of Elasticity of Metals and Non-Metals. Reference Book) (Kiev: Naukova Dumka, 1982)
139. Bullough R *Ann. Chim.* **9** 255 (1984)
140. Kuramoto E *J. Nucl. Mater.* **122** 422 (1984)
141. Charai A, Boulesteix C *Phys. Status Solidi A* **80** 333 (1983)
142. Palatnik L S et al. *Kristallografiya* **32** 445 (1987)
143. Malhotra S G et al. *J. Appl. Phys.* **79** 6872 (1996)